Coastal Engineering 208 (2026) 105016

Contents lists available at ScienceDirect

Coastal Engineering

journal homepage: www.elsevier.com/locate/coastaleng

Wave focusing over tidal turbine wakes

Samuel Draycott [a,*], Hannah Mullings [a], Pablo Ouro [a,b], Peter Stansby [a], Tim Stallard [a]

[a] School of Engineering, University of Manchester, Manchester, M13 9PL, United Kingdom
[b] Galicia Supercomputing Centre (CESGA), Santiago de Compostela, 15705, Spain

ARTICLE INFO

Keywords:
Tidal turbine wakes
Wave–current interaction
Wave refraction
Wave focusing

ABSTRACT

Tidal stream turbines operate in combined wave–current conditions and the downstream wakes that develop due to momentum extraction can modify wave conditions through Doppler shift and refraction. We study this using a wave-ray tracing approach with an effective depth-integrated current representing idealised wakes at rated operation. Four lateral layouts are examined for full-scale turbines (radius R = 9 m, D = 18 m) in $4R$ water depth with a typical freestream velocity U_0 = 2.5 ms^{-1}. We simulate approximately 2500 regular wave cases, spanning periods 4–16 s and a range of relative headings to assess wave amplification fields (averaged over $R \times R$ windows), before creating weighted averages representing irregular and directionally spread wave fields. Peak amplification for regular waves reaches $> 3A_0$ (with A_0 the incident wave amplitude) for near-opposing incidence and around $2.5A_0$ for near-following conditions. However, spatial integration reveals that while extreme amplifications ($> 1.5A_0$) are highly localised ($< 100D^2$), moderate amplifications ($1.1A_0$) persist over expansive regions (up to $1000D^2$). Furthermore, sensitivity analysis demonstrates that this focusing mechanism is highly robust; despite $\pm 40\%$ variations in freestream velocity and wake deficit, peak amplifications remain remarkably stable. Unidirectional irregular seas smooth focusing ($2.2A_0$ maximum) and directional spreading reduces amplification further to between $1.75A_0$ and $1.35A_0$ for moderate and large spreading respectively. Theoretical transmission errors are calculated to be small ($< 10\%$) for most wave conditions, and comparison against a phase-resolved Boussinesq model confirms that the spatial focusing regions are consistent. While the omission of diffraction leads to local amplitude over-predictions at focal points, the ray-tracing approach is shown to be a highly efficient and conservative screening tool for tidal array design. These results indicate that the wave-induced loading of turbines within an array could differ considerably from an isolated turbine, with amplification magnitude and location dependent on array geometry, turbine operation and site characteristics meriting further study.

1. Introduction

Tidal stream power is a highly dense, predictable, renewable energy source. Recent studies estimate the practical resource in the UK alone to be around 34 TWh/year (Coles et al., 2021). To extract this, modern tidal stream turbines (TSTs) are designed to generate energy in tidal channels using horizontal-axis rotors. Several full-scale prototypes and small arrays have now operated successfully at energetic sites including the MeyGen project and the European Marine Energy Centre (e.g. Sellar et al., 2018), confirming technical feasibility. Ongoing efforts are focused on scaling from single devices to multi-turbine farms, where interactions between turbines, their wakes, and the surrounding flow increasingly determine overall farm efficiency and turbine loading (Nishino and Willden, 2012; Ouro and Nishino, 2021; Mullings et al., 2024). Understanding these array-scale hydrodynamics is therefore critical to the effective design and operation of future commercial farms (Stansby and Ouro, 2022).

The interaction between surface gravity waves and tidal stream turbines has been widely studied for single devices. In these combined wave–current conditions, the unsteady wave-induced orbital velocities modulate the instantaneous inflow to the rotor, leading to potentially large fluctuations in thrust, torque, and power. Numerous laboratory experiments have characterised these effects under regular wave conditions, showing systematic dependencies on wave amplitude, steepness, and frequency (and hence relative depth kd where k is the wavenumber and d the depth) (Barltrop et al., 2006; Gaurier et al., 2013; de Jesus Henriques et al., 2014; Draycott et al., 2019b; Gaurier et al., 2020). Comparisons with blade element momentum theory (BEMT) and simplified inflow models have demonstrated that much of the wave-induced loading variation can be captured by accounting for local wave kinematics (Barltrop et al., 2006; Faudot and Dahlhaug, 2012; Galloway et al., 2014). Additional sensitivities have been explored e.g. with respect to wave phase (Lust et al., 2013), turbine

---

[*] Corresponding author.
E-mail address: samuel.draycott@manchester.ac.uk (S. Draycott).

https://doi.org/10.1016/j.coastaleng.2026.105016
Received 16 December 2025; Received in revised form 11 March 2026; Accepted 1 April 2026

submergence (Luznik et al., 2013), and control strategy (Ordonez-Sanchez et al., 2019; Martinez et al., 2020; Nambiar et al., 2021), revealing complex but generally predictable responses. Understanding has subsequently been extended to irregular sea states, showing that realistic wave spectra modifies load distributions, and under certain conditions introduces additional high-frequency components associated with blade rotational sampling (Draycott et al., 2019c, 2020b,a), also present in regular conditions. Under extreme focused wave events, peak thrust and power output can exceed mean values by up to 85% and 200% respectively (Draycott et al., 2019a). Together, these findings indicate that wave loading on individual TSTs is a critical design load condition. Whilst loading in such combined conditions is now relatively well understood through experiments, the wave conditions that define peak loading have received less attention. Other experimental works have shown that waves can accelerate wake recovery (Stallard et al., 2013; Zang et al., 2023) and modify turbulence intensity and wake structure (Zhang et al., 2021).

Numerical simulations, predominantly using Reynolds-averaged Navier Stokes (RANS)-based models (S.C. Tatum et al., 2016; S. Tatum et al., 2016; Apsley et al., 2018; Li et al., 2021), have been shown able to capture key loading and flow behaviour. These studies, however, remain limited in representing the interactions between waves and turbulent structures, motivating the use of higher-fidelity Large-Eddy Simulation (LES) approaches (Posa and Broglia, 2021, 2022). Recent LES studies have begun to resolve the detailed physics of wake-wave interaction, showing how waves modulate vortex convection, vertical momentum transport, and the recovery of the velocity deficit (Hurubi et al., 2025). In particular, in Ouro et al. (2024) it was demonstrated that surface waves modify the evolution of turbine tip vortices and enhance wake recovery through increased vertical mixing, building on Stallard et al. (2023). Despite these advances, knowledge of wave effects remains largely confined to single-device studies, leaving open questions about how such interactions scale and couple across multiple turbines within arrays.

In terms of understanding array considerations, early experimental work examined wake recovery and turbine interactions under current-only flow, including studies of single-rotor wakes of relevance to array design, showing sensitivity to device spacing and inflow turbulence (Myers and Bahaj, 2012; Stallard et al., 2013; Olczak et al., 2016). Subsequent laboratory campaigns have explored closely spaced configurations and the resulting flow acceleration and load variability between turbines e.g. Noble et al. (2020) provided a detailed assessment of flow, performance, and loading for three turbines in a closely spaced array, which has been recently simulated numerically (Apsley, 2024) using a RANS model. Collectively, these studies have helped to characterise near-wake merging, vertical asymmetry, and lateral deflection of wakes that occur when multiple devices operate in proximity.

At larger scales, numerical and analytical models have been used to investigate wake superposition, array blockage, and channel-scale effects. Depth-averaged and actuator-disc frameworks have clarified the relationships between device spacing, blockage ratio, and array efficiency (Nishino and Willden, 2012; Adcock et al., 2013). High-fidelity large-eddy simulations have further resolved wake interactions and momentum recovery within turbine arrays (Ouro et al., 2019; Ouro and Nishino, 2021). Adjoint-based optimisation and coupled hydrodynamic models have also been applied to assess the performance of large turbine farms and their feedback on tidal channel dynamics, providing a basis for site-scale optimisation and environmental assessment (Funke et al., 2014). Despite these advances, most array-scale investigations have assumed steady (or pseudo-steady) current conditions and neglected surface waves. Existing studies therefore capture the mean flow coupling between turbines but overlook potential modulation of the wave field by turbine wakes and the feedback of refracted or focused waves on local loading and array performance.

Currents are known to modify surface gravity waves through Doppler shift and refractive effects, with wave amplitudes adjusting in accordance with the conservation of wave action (Johnson, 1947; Jonsson and Wang, 1980; Peregrine and Jonsson, 1983). Through wide-area spectral wave modelling it is also known that strong tidal currents can induce significant temporal and spatial variability of the wave field (e.g. Mackay and Hardwick, 2022; Sabatino et al., 2016) and that waves can significantly alter the tidal resource (Hashemi et al., 2015). When current gradients are strong, these processes can lead to dramatic focusing of wave energy and enhanced local steepness. A well-known example is the Agulhas Current off the East coast of South Africa, where opposing flows substantially increase significant wave heights and the probability of rogue waves through current-induced refraction (de Leon and Soares, 2022; Quilfen et al., 2018; Barnes and Rautenbach, 2020). The lack of existing large scale tidal farms exposed to waves has limited opportunities to observe equivalent processes, and the potential for turbine wakes to refractively focus or deflect surface waves remains unexplored.

The importance of coupled wave–current dynamics is increasingly recognised, prompting advances in both theoretical and numerical modelling frameworks. Recent theoretical developments extend understanding to account for horizontal and vertical current shear (Li and Ellingsen, 2019; Li and Chabchoub, 2024), while there have also been parallel advances in numerical modelling at different scales (Babanin et al., 2017; Yang et al., 2023a,b). Analytical progress has also been made in clarifying the joint roles of current and bathymetric gradients in modulating wave-ray curvature and refraction, as recently demonstrated (Halsne and Li, 2025). Collectively, these studies demonstrate that current jets and horizontal shear can refractively focus surface waves, analogous to the focusing of light by optical lenses, which is supported by limited, challenging, experiments (MacIver et al., 2006; Toffoli et al., 2011). By extension, the velocity deficits produced by tidal-turbine wakes may similarly concentrate wave energy within an array, yet this remains largely unexplored. Early work has shown the refractive effects to be dominant in wave focusing over turbine wakes (Olczak, 2016) (see Chapter 7, Figs. 7.9 and 7.12).

In this paper, we show that wakes generated by TST arrays cause directional focusing of waves, resulting in localised wave amplification that can adversely affect down-wave turbines in arrays (and even turbines whose wake is modifying the waves). We apply a wave ray-tracing approach based on the Wentzel–Kramers–Brillouin (WKB) approximation (Halsne et al., 2023), treating wave propagation geometrically through a spatially varying current. This modelling approach will capture wave refraction effects but omit several other physical aspects which are expected to be less significant for the majority of wave conditions of interest (explored in Section 4). We use an effective, depth-integrated velocity field that captures the portion of the vertical shear profile ‘felt’ by waves, and use a three-zone wake model representative of typical turbine operation. We then assess regular wave amplification due to directional focusing as a function of wave period, wave heading and turbine array layout. This is then extended to unidirectional irregular waves and directionally spread seas. Crucially, we evaluate not only the absolute peak amplifications but also the spatial footprint of these hazards to contextualise array-scale risk. The remainder of the paper is laid out as follows: Section 2 details the modelling approach, Section 3 presents example results, amplification maps and spatial analysis for regular, irregular, and directionally spread seas. Section 4 discusses the sensitivity of focusing to flow parameters, discusses the limitations (including estimates of the errors from the wave ray tracing approach taken), provides an initial comparison to a phase-resolved Boussinesq wave model (FUNWAVE-TVD) (Shi et al., 2012), and suggestions for future study including hybrid modelling approaches. Finally, concluding remarks are offered in Section 5.

2. Methodology

2.1. Wave ray tracing

Throughout we assume linear surface gravity waves, a steady background current represented by a depth-integrated effective velocity field, and one-way coupling (currents affect waves but not vice versa). The wave ray tracing method presented in Halsne et al. (2023) solves the wave ray equations derived under the Wentzel–Kramers–Brillouin (WKB) approximation, i.e. assuming slow variations in wave properties over distances on the order of wavelength L. The method accounts for wave refraction due to ambient currents and variable bathymetry. The wave ray equations in two dimensions for a steady current field are:

$$\frac{d\mathbf{x}}{dt} = \mathbf{c}_g + \mathbf{U}, \tag{1}$$

$$\frac{d\mathbf{k}}{dt} = -\nabla_h \sigma - \mathbf{k} \cdot \nabla_h \mathbf{U}, \tag{2}$$

$$\frac{d\omega}{dt} = 0, \tag{3}$$

Here, $\mathbf{x} = (x, y)$ denotes the time-dependent position of the wave ray, and $\mathbf{k} = (k_x, k_y)$ is the wavenumber vector with magnitude $k = |\mathbf{k}|$. The intrinsic (relative) angular frequency is $\sigma = \sqrt{gk\,\tanh(kd)}$, where d is the water depth, and the group velocity is $\mathbf{c}_g = \partial\sigma/\partial\mathbf{k}$. The ambient current velocity is $\mathbf{U} = (U, V)$, so the absolute angular frequency is $\omega = \sigma + \mathbf{k} \cdot \mathbf{U}$. Finally, ∇_h denotes the horizontal gradient operator.

These equations describe the advection of the wave group (Eq. (1)), the evolution of the wavenumber (refraction, Eq. (2)), and the conservation of frequency (i.e. number of waves, Eq. (3)). Note that the absolute frequency ω remains constant but σ and k vary along the rays if there are changes to current velocity or depth. The equations are solved numerically using a fourth-order Runge–Kutta scheme via the Ocean wave tracing v.1 package (Halsne et al., 2023) (available at https://doi.org/10.5281/zenodo.7602540).

To ensure reproducibility and numerical stability, the velocity field for each case is discretised over a large computational domain extending from $-30D$ to $+30D$ in the global streamwise (x) direction and $-40D$ to $+40D$ in the transverse (y) direction, using a grid resolution of $N_{grid} = 600$ points along each axis. Waves are introduced into the domain via an evenly spaced injection of $N_{rays} = 1000$ rays along the upwave boundary. A comprehensive sensitivity analysis confirming the numerical convergence of the model with respect to both the grid resolution (N_{grid}) and the number of injected rays (N_{rays}) is detailed in Appendix A.

The ray trajectories are integrated over $N_T = 1500$ time steps. To ensure all rays fully traverse the computational grid, the total simulation duration (T_{sim}) is dynamically calculated for each case as 1.2 times the theoretical crossing time of the slowest wave component (determined using the minimum absolute group velocity across the current field). The resulting integration time step ($\Delta t = T_{sim}/N_T$) adapts to the specific wave–current conditions. This ensures the Courant number remains $C = W\frac{\Delta t}{\Delta r} < 1$ across all simulations, where $W = \max|\mathbf{U}| + \max(c_{g,t=0})$ is the maximum advection velocity evaluated at the upwave boundary and $\Delta r = \sqrt{\Delta x^2 + \Delta y^2}$.

Because the wave-ray tracing approach operates by integrating ordinary differential equations along Lagrangian ray paths, numerical wave reflection at the outer boundaries does not occur. Rays simply advect through the spatially varying current field until they naturally exit the domain. Consequently, no artificial boundary damping or sponge layers are required. Furthermore, the extensive streamwise domain ensures that the primary refractive focusing zones are fully captured within the grid before the rays exit. For full package implementation details, the reader is referred to Halsne et al. (2023).

The wave ray tracing assumptions (i.e. WKB approximation) are not strictly valid when large variations in wavenumber happen over small spatial scales, as is the case for some of the cases studied in this paper. This means that some physical processes such as wave transmission/reflection are not captured close to sharp transitions, e.g. the near wake region. It is worth noting that there are promising results for waves deflecting over sharp velocity transitions presented in Halsne et al. (2023), with errors in the order of 1% which reduces with reducing Courant number. Thus, the practical integration of the wave ray tracing equations can still give useful predictions of wave refraction as is the focus of this paper. The expected errors associated with using this method for this problem are further assessed in Section 4.

2.2. Wake model

In order to solve the wave ray tracing equations over turbine wakes, we need to formulate a simplified yet representative wake model. To do this we split the wake into three regions depending on the ratio between the streamwise distance x downstream of the turbine of diameter D, i.e. x/D: (i) the near wake region $x < 2D$, (ii) the mid-wake region $2D < x < 8D$, and (iii) the far wake region $x > 8D$. The peak velocity deficit $\Delta U(x)$ is therefore defined based on three different functions f_i representing each of these zones:

$$\Delta U(x) = \begin{cases} f_1(x) \cdot U_0, & x < 2D \\ f_2(x) \cdot U_0, & 2D \le x < 8D \\ f_3(x) \cdot U_0, & x \ge 8D \end{cases} \tag{4}$$

To approximate the wake structure in these three zones, we use the experimental work of Stallard et al. (2015) and Stansby and Stallard (2016), and hence the wake structure will be representative of turbines operating in all speeds up to and including rated speed in comparable relative channel geometries. We assume a constant uniform depth.

2.2.1. Transverse profile

The wake profile in the transverse (y) direction, is given as a Gaussian for each turbine (subscript T):

$$\mathcal{G}(x, y) = \sum_{t=1}^{N_t} \exp\left(-\ln 2 \left(\frac{y - y_T}{y_{1/2}(x)}\right)^2\right) \tag{5}$$

where N_t is the total number of turbine wakes modelled and y_T is the y position of the centre of the rotor for turbine t. The transverse half-widths are given by:

$$y_{1/2}(x) = \begin{cases} f_{1y}(x)\,\dfrac{D}{2}, & x < 2D \\ f_{2y}(x)\,\dfrac{D}{2}, & 2D \le x < 8D \\ f_{3y}(x)\,\dfrac{D}{2}, & x \ge 8D \end{cases} \tag{6}$$

2.2.2. Vertical profile

The transverse wake is effectively unconstrained and as such can remain as a self-similar Gaussian over the full range of x positions. For the vertical profile, due to the finite depth, this is not applicable, and as noted in Stallard et al. (2015), the vertical velocity profile becomes similar to the incoming velocity profile (approximately uniform) after around $6D \rightarrow 8D$. The vertical profile is therefore modelled using a linear smoothing function $w(x)$ between a Gaussian and a uniform profile:

$$\mathcal{Z}(x, z) = (1 - w(x)) \exp\left(-\ln 2 \left(\frac{z - z_T}{z_{1/2}(x)}\right)^2\right) + w(x) \tag{7}$$

where z_T is the turbine hub height and is set to $z_T = -d/2$ for all turbines and for all cases, i.e. the rotor is centred at mid-depth. Due to observed axisymmetric wakes in the near-wake region (e.g. Stallard et al., 2015), the shape of the Gaussian in z is set to be equivalent to the shape in y, i.e. $z_{1/2}(x) = y_{1/2}(x)$. The smoothing function $w(x)$ is given by:

$$w(x) = \text{clip}\left(\frac{x/D - (x_{centre} - \delta)}{2\delta}, 0, 1\right) \tag{8}$$

where the centre of the smoothing function is x_{centre} and 2δ is the function width. The 'clip' function limits the outputs of $w(z)$ to be between 0 and 1. We set $x_{centre} = 6$ and $\delta = 2$ to be approximately consistent with observations from Stallard et al. (2015).

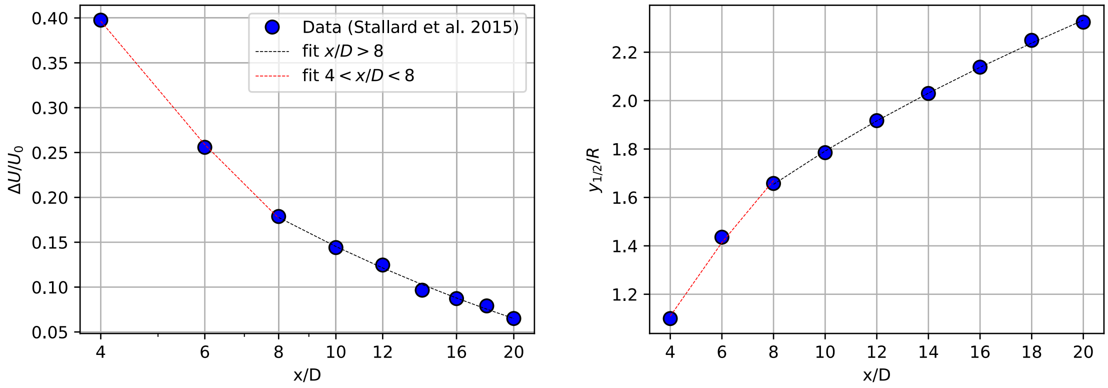

Fig. 1. Coefficient fit to Stallard et al. (2015) for the peak velocity deficit ΔU (left) and transverse profile half-width $y_{1/2}$ (right). The fit for $4D < x < 8D$ is applied over the mid-wake region whilst the fit for $x > 8D$ is applied for all locations with $x > 8D$.

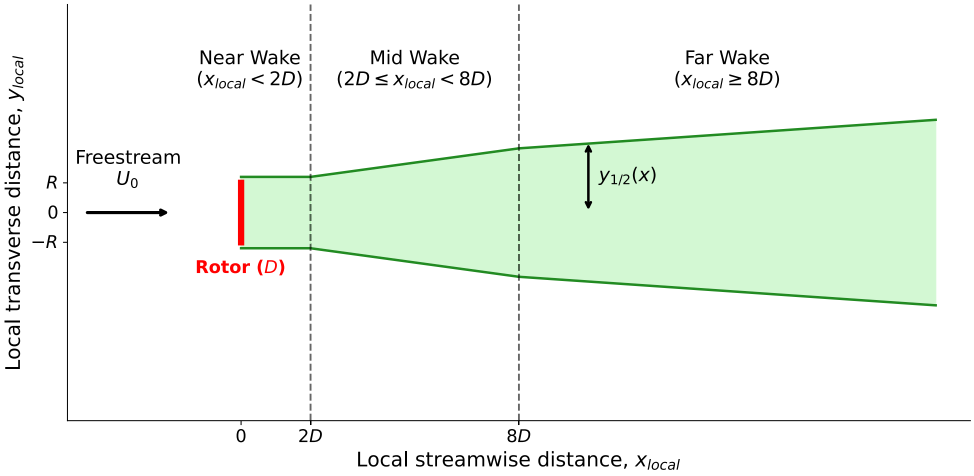

Fig. 2. Schematic of the idealised three-zone wake model, illustrating the near, mid, and far wake regions. The variables are defined in the local turbine reference frame (x_{local}, y_{local}), where the freestream current U_0 flows in the positive x_{local} direction.

2.2.3. *Functional forms*

As mentioned, the wake model uses three zones. In the near wake region (i), we assume an asymmetric wake structure which is constant over $0D \rightarrow 2D$ based on values for the mid-wake at $x = 2D$. The mid-wake (ii) is defined as an expanding wake, based on a new linear fit to the data presented in Stallard et al. (2015) over $4D < x < 8D$, which is assumed to hold over $2D < x < 8D$. This linear fit is presented as a red line in Fig. 1. The far wake is modelled using the coefficients presented in Stallard et al. (2015) for $8D < x < 20D$ (black line in Fig. 1) and is assumed to hold for all $x > 8D$. The coefficients for each zone are detailed in Table 1. To model arrays of turbines, the wake deficit profiles for individual turbine wakes are linearly superposed, an approach that is widely used in the wind industry and shown to give good predictions for tidal stream turbine arrays when the array blockage is low (Stansby and Stallard, 2016; Olczak et al., 2016; Ouro et al., 2023).

A schematic defining these three geometric wake regions and the relevant variables in the local turbine reference frame (x_{local}, y_{local}) is provided in Fig. 2.

2.2.4. *Total and effective velocity fields*

Based on the above, the streamwise velocity field is given by:

$$U(x, y, z) = U_0 - \Delta U(x) \cdot \mathcal{G}(x, y) \cdot \mathcal{Z}(x, z) \tag{9}$$

where the induction region is neglected and therefore in the region upstream of the turbines ($x < 0$ in the reference frame of the turbine):

$$U(x < 0, y, z) = U_0 \tag{10}$$

Table 1
Functions and coefficients for peak velocity deficit and transverse half-width.

Zone	Functions	m	c
1: Near wake ($x < 2D$)	$f_1(x) = m_{U1}(2)^{-\frac{1}{2}} + c_{U1}$ $f_{1y}(x) = m_{y1}\sqrt{2} + c_{y1}$	$m_{U1} = m_{U2}$ $m_{y1} = m_{y2}$	$c_{U1} = c_{U2}$ $c_{y1} = c_{y2}$
2: Mid wake ($2D \leq x < 8D$)	$f_2(x) = m_{U2}(x/D)^{-\frac{1}{2}} + c_{U2}$ $f_{2y}(x) = m_{y2}(x/D)^{\frac{1}{2}} + c_{y2}$	$m_{U2} = 1.5$ $m_{y2} = 0.676$	$c_{U2} = -0.353$ $c_{y2} = -0.242$
3: Far wake ($x \geq 8D$)	$f_3(x) = m_{U3}(x/D)^{-\frac{1}{2}} + c_{U3}$ $f_{3y}(x) = m_{y3}(x/D)^{\frac{1}{2}} + c_{y3}$	$m_{U3} = 0.864$ $m_{y3} = 0.412$	$c_{U3} = -0.126$ $c_{y3} = 0.5$

In a coordinate system with the streamwise direction along the positive x direction, the transverse velocity $V(x, y, z)$ is assumed to be zero. The implications of this are discussed later in Section 4.

Effective velocity field. The wave ray tracing model requires on a 2D velocity field $\mathbf{U}(x, y)$ and as such we need to define an effective 2D field. To do this, we use the velocity of an equivalent uniform current defined in Hedges and Lee (1992), which is the uniform current which produces the same wavelength as the actual depth-varying current:

$$\mathbf{U_e(x, y)} = \frac{1}{\epsilon L}\int_{-\epsilon L}^{0} U(x, y, z)dz \tag{11}$$

where $\mathbf{U_e}$ is the effective current vector and $L = 2\pi/k$ is the wavelength. ϵ is a factor which depends mostly on kd. Given the wavelength will vary depending on the direction of the waves relative to the current field, which is one of the things we need to solve for with the wave

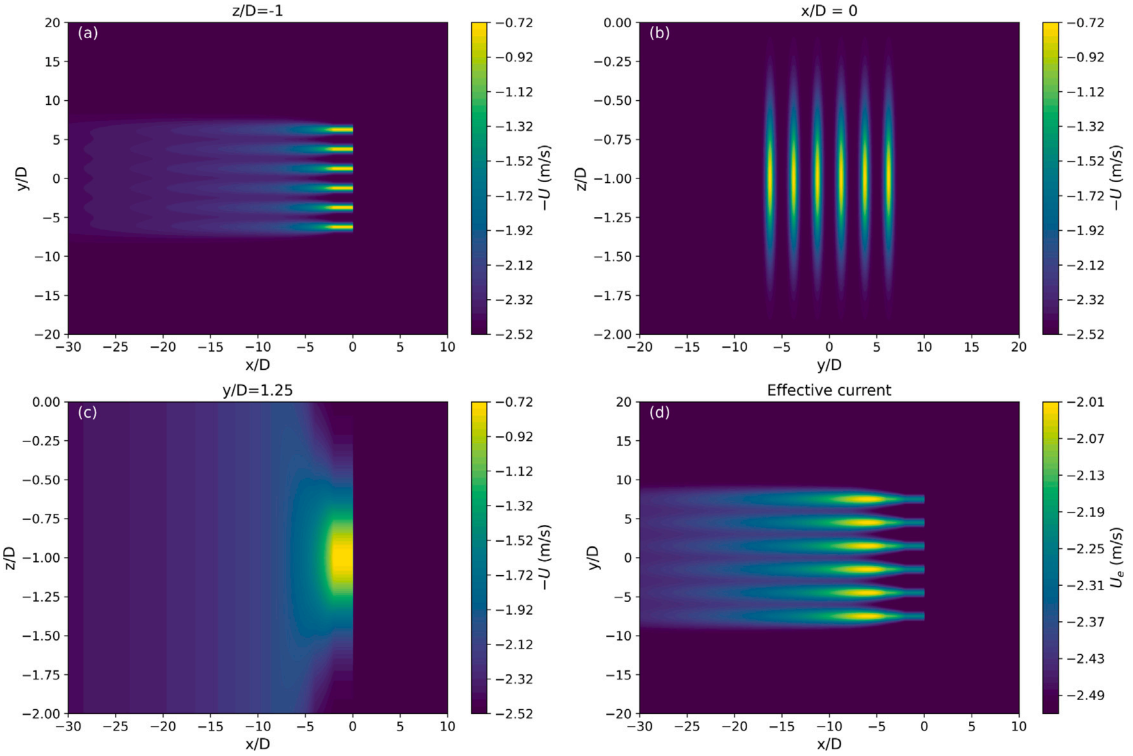

Fig. 3. Example velocity field with 6 turbines spaced $2.5D$ apart (T4 as defined in Fig. 4) and with a freestream velocity $U_0 = 2.5$ m/s, with 7 s waves opposing the current direction (waves travelling left to right). The plot shows: (a) the x-y plane at $z/D = -1$ (mid-depth), (b) the y-z plane at $x/D = 0$, (c) the x-z plane at $y/D = 1.25$ (along the axis of one turbine wake), and (d) the effective velocity computed from Eq. (11). The velocity presented on panels (a)–(c) is $-U$ to facilitate comparison to U_e on panel (d).

tracing calculations, the approximation presented in Hedges and Lee (1992) is used, whereby:

$$\epsilon L \approx \frac{\tanh k_0 d}{k_0} \tag{12}$$

where k_0 is the wavenumber in the absence of current, calculated by solving the linear dispersion relation:

$$\omega^2 = g k_0 \tanh k_0 d \tag{13}$$

where $\omega = 2\pi/T$ is the absolute angular frequency with T the wave period, d is the water depth, and g is acceleration due to gravity. This is an approximation, but avoids a complex iterative process to refine the estimate based on intermediate estimates of the instantaneous wave ray directions based on an iteratively updated depth integration. This 2D effective velocity field is used for the ray tracing calculations. Limitations of this approach are discussed further in Section 4.

An example velocity field including the approximate wakes, and the effective horizontal velocity from the depth-integration (Eq. (11)) for a 7 s wave is presented in Fig. 3. It is evident that for this wave period ($k_0 d = 2.97$) the wave does not really interact with the near wake, despite the much larger velocity deficit, but experiences a larger deficit further along the wake due to the wake expansion in the z direction. This highlights an interesting trade-off: the lower period waves will be more affected by the change in current due to their lower group velocities, but due to the higher wavenumbers will effectively not interact with the lowest velocities in the near and mid wake. Conversely longer, higher period, waves will interact with a larger velocity deficit but be less affected due to their higher group velocities.

Note that while the idealised wake model is defined using a local turbine-aligned coordinate system (x_{local}, y_{local}) as depicted in Fig. 2, all wave-ray tracing computations and subsequent results use a global, wave-centred coordinate system (x, y). In this global system, x always increases from left to right, with waves injected nominally from the left boundary. We consider three canonical mean headings relative to the current: following ($\bar{\theta}_{\mathrm{rel}} = 0°$), opposing (180°), and perpendicular (90°). For each of these three cases we rotate the velocity field once so that the nominal wave propagation is along $+x$ (left to right) and the current is oriented accordingly. For instance, under opposing wave conditions, the local wake velocity field is rotated by 180° such that the freestream current flows in the $-x$ direction and the wake extends to the left of the origin (e.g. as shown later in Fig. 3), while waves continue to propagate in the $+x$ direction.

Small departures from the mean (the ±20° sweeps described in Section 2.3) are then imposed by specifying waves from the left boundary at headings $\bar{\theta}_{\mathrm{rel}} \pm \delta$, $\delta \in [0, 20°]$, without further rotating the velocity field. This approach avoids the need for interpolation and allows for a consistent averaging window to be employed across wave conditions Thus, throughout, waves propagate nominally left-to-right: "near-following/near-opposing/near-perpendicular" refers to these ±20° variations about the nominal mean orientation.

2.3. Analysis

The main focus of the analysis is on identifying the wave amplification that occurs due to interaction of the wave-field with the spatially varying (effective) velocity field developed by tidal turbines. The magnitude and location of wave amplification are both of interest as this may represent the worst-case loading conditions for which a turbine would need to be designed. We therefore focus on the ratio $A(x, y)/A_0$ where A_0 is the incident amplitude and $A(x, y)$ is the local amplitude. The wave ray tracing code does not solve for wave amplitude, and as such we use the ray density, calculated as the number of rays in a cell (see Rapizo et al., 2014). We define the relative ray density as the sum of rays in a given area, normalised by the value at cell [1,1] (bottom left

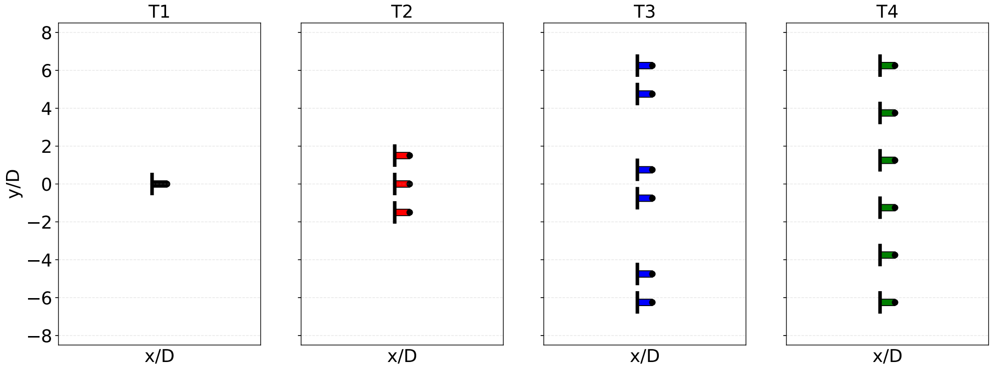

Fig. 4. Turbine configurations assessed.

corner) which is set to always be part of the undisturbed flow before interaction with the wakes.

$$\rho_{ray}(x,y) = \frac{\sum_{r\in\mathcal{R}} \mathbf{1}_{\Omega(x,y)}(r)}{\sum_{r\in\mathcal{R}} \mathbf{1}_{\Omega_{1,1}}(r)}. \tag{14}$$

where $\mathcal{R}$ is the set of rays, $\Omega(x,y)$ is the $R \times R$ box (with $R = D/2$) centred at (x,y), $\Omega_{1,1}$ is the box for cell location [1,1] (upwave) of the same size, and

$$\mathbf{1}_{\Omega}(r) = \begin{cases} 1, & \text{if the trajectory of ray } r \text{ intersects } \Omega, \\ 0, & \text{otherwise.} \end{cases} \tag{15}$$

The region size $R \times R$ is chosen since this is most relevant for the turbine. Smaller bins would give larger local peak amplifications, but arguably not on a scale of relevance for the wave-induced loading on a tidal turbine rotor which is typically defined by the thrust coefficient based on rotor area, whereas it is noted that smaller regions could be of relevance for loading experience by individual blades.

The normalised ray density $\rho_{ray}(x,y)$ effectively describes a ratio of the relative energy, and as such, the relative wave amplitude can be approximated as:

$$\frac{A(x,y)}{A_0} = \sqrt{\rho_{ray}(x,y)}, \tag{16}$$

assuming that locally linear wave theory applies and therefore energy density scales with A^2. Here 'amplification' refers to geometric focusing inferred from ray density. Local amplitude adjustments due to conservation of wave action across velocity gradients are not included in Eq. (16) and are assessed separately in Section 4.2.

The code solves for a single frequency and incident angle, and so to simulate realistic irregular seas, average wave amplification fields $A(x,y)_{irreg}/A_0$ are generated by weighting individual frequency and angle combinations by their relative amplitudes within the spectrum. For this analysis we assume JONSWAP frequency spectra $S(f)$ (Hasselmann et al., 1973), with a Gaussian frequency-independent directional spreading function $D(\theta)$, where directional spreading is controlled by the standard deviation σ_θ (see e.g. McAllister et al., 2024; Stansby et al., 2022). The resulting directional energy spectrum $E(f,\theta) = S(f)D(\theta)$, and the component amplitudes can be computed for frequency component i and directional component j using $A_{i,j} = \sqrt{2E(f_i,\theta_j)\Delta F \Delta\theta}$, and as such the weighted normalised wave amplitude fields are calculated by:

$$\begin{aligned} A(x,y)_{irreg}/A_0 &= \sum_{i=1}^{N_f}\sum_{j=1}^{N_\theta}\left(\frac{A(x,y)}{A_0}\right)_{i,j}\frac{A_{i,j}}{\sum A_{i,j}} \\ &= \sum_{i=1}^{N_f}\sum_{j=1}^{N_\theta}\left(\frac{A(x,y)}{A_0}\right)_{i,j}\frac{\sqrt{E(f_i,\theta_j)}}{\sum\sqrt{E(f_i,\theta_j)}} \end{aligned} \tag{17}$$

Finally, to contextualise the spatial footprint of these effects across the array, we integrate these 2D fields to compute the total normalised domain area ($Area/D^2$) over which the local amplitude exceeds specific thresholds.

2.4. Test cases

The main set of test cases, and associated analysis in Section 3, focus on the sensitivity to wave conditions for a small set of wake scenarios: a single turbine wake (T1), a row of 3 turbines with 1.5 D spacing (T2), 6 turbines in pairs with intra-pair spacing of 1.5 D and inter-pair spacings of 4 D (T3), 6 turbines with spacings of 2.5 D (T4). T4 is designed to have the same total width as T3. These are depicted in Fig. 4.

For the primary spatial analysis, we define a baseline freestream velocity U_0 of 2.5 m/s, typical of peak values at tidal turbine sites, and associated with close to largest velocity gradients and therefore refractive focusing effects. To assess how sensitive results are to variations in the flow field, a parametric sensitivity sweep varying both U_0 and the wake velocity deficit ΔU is also conducted, as detailed later in Section 4.1. The aim is to assess how waves are refracted by the spatially varying steady velocity field and to identify regions of amplification that may affect the loading or placement of down-wave turbines (not-modelled). A range of wave periods and wave headings are assessed for each turbine array layout. For each configuration we assess results for a range of wave periods T from 4 to 16 s in 1 s increments, other than for opposing conditions where wave propagation is blocked by the current when $T \lesssim 6.4$ s, i.e. when the absolute (ground-frame) ray speed satisfies $\frac{d\mathbf{x}}{dt} = \mathbf{c}_g + \mathbf{U} \approx \mathbf{0}$, so we only compute from 7 s to 16 s. For every period and configuration, we also compute results for a range of incident angles for near following conditions ($\theta_{rel} = 340° : 2.5° : 20°$), near opposing conditions ($\theta_{rel} = 160° : 2.5° : 200°$), and near perpendicular ($\theta_{wave} = 70° : 2.5° : 110°$) conditions. This enables an assessment of the effects of non-collinearity for regular wave conditions, and also enables the effect of directional spreading to be assessed (see Eq. (17)). A total of 2448 regular wave cases are computed, and these results are combined in post-processing to assess the smoothing effects induced by more realistic irregular waves.

3. Results

3.1. Regular waves

We first assess area-averaged wave amplification over windows of $R \times R$ for regular wave conditions, where geometric (refractive) focusing is expected to be stronger than for irregular wave conditions.

Example ray fields (every fifth ray plotted) are shown in Fig. 5 for $T = 10$ s and $\theta_{rel} = 190°$ (i.e. 10° from strictly opposing) across all four turbine array layouts. Despite differing layouts, rays converge on similar bands flanking the turbines, indicating robust refractive focusing driven by the wake-induced current gradients. The corresponding normalised amplitude maps are given in Fig. 6 for this condition. Peak local amplitudes exceed $2.5 \times A_0$, with only modest sensitivity to layout overall. The largest peaks occur for layout T4, consistent with its more coherent far-wake structure formed by merging neighbouring wakes.

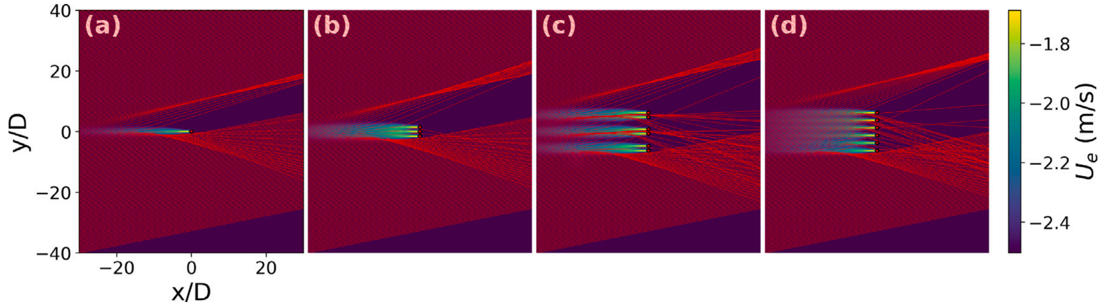

Fig. 5. Wave rays for different turbine configurations, for T = 10 s waves at 10 deg relative to opposing the mean current direction i.e. θ_{rel} = 190°. Shown for (a) T1, (b) T2, (c) T3, (d) T4. Turbine locations are shown as red circles. The value of U_e is shown underneath the wave rays. Note only every 5 rays are plotted for visualisation.

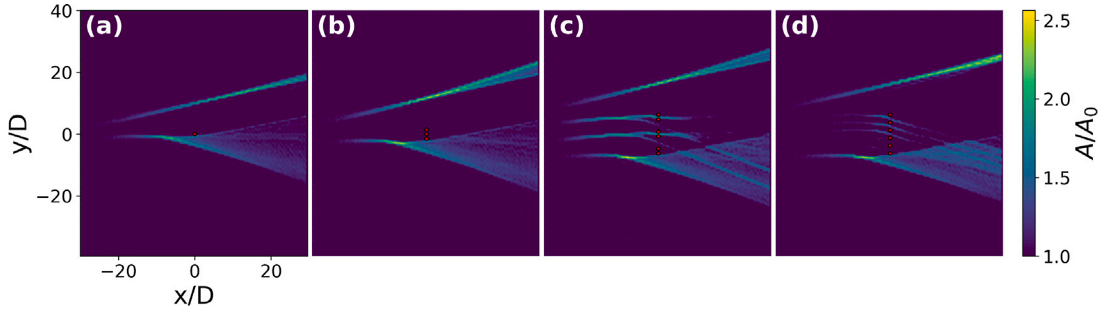

Fig. 6. Normalised wave amplitude for different turbine configurations, for T = 10 s waves at 10 deg relative to opposing the mean current direction i.e. θ_{rel} = 190°. Shown for (a) T1, (b) T2, (c) T3, (d) T4. Turbine locations are shown as red circles.

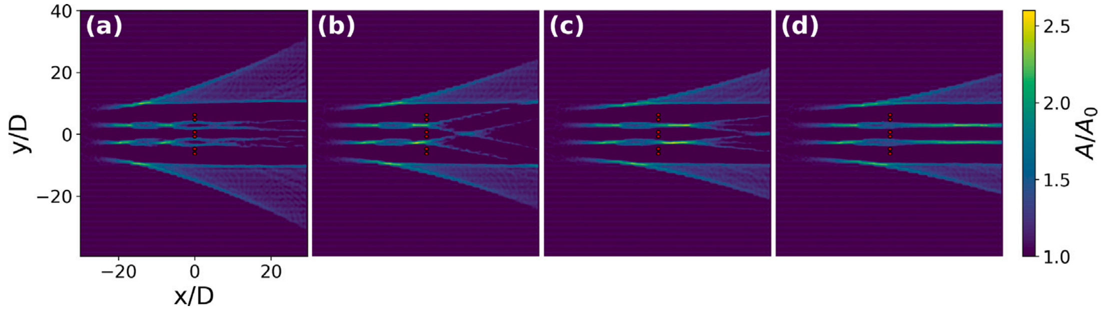

Fig. 7. Normalised wave amplitude for different wave periods over turbine configuration T3, for waves opposing the mean current direction i.e. θ_{rel} = 180°. Shown for (a) T = 8 s, (b) T = 10 s, (c) T = 12 s, (d) T = 14 s. Turbine locations are shown as red circles.

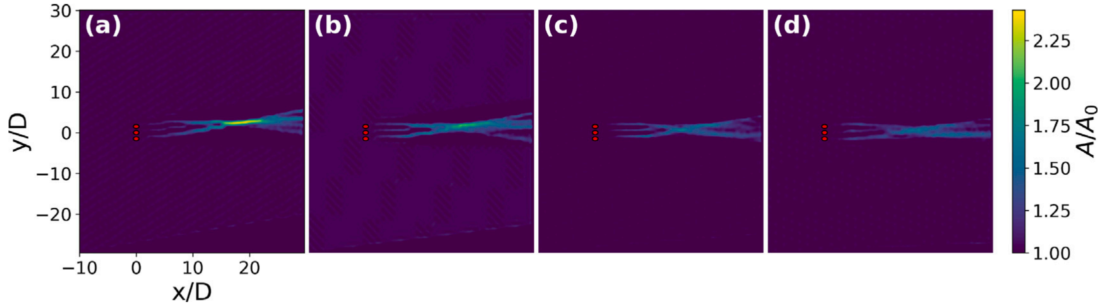

Fig. 8. Normalised wave amplitude for different wave angles over turbine configuration T2, for T = 6 s waves close to following the mean current direction. Shown for (a) θ_{rel} = 20°, (b) θ_{rel} = 15°, (c) θ_{rel} = 10° (d) θ_{rel} = 5°. Turbine locations are shown as red circles.

Equivalent amplification plots are presented in Figs. 7 and 8 highlighting sensitivity to wave period and angle respectively. Fig. 7 examines period sensitivity for layout T3 for waves opposing current (θ_{rel} = 180°) for T = 8–14 s. Longer wave periods refract less (longer wavelengths, higher c_g), yet localised regions of large amplification persist, showing that weaker curvature of the wave rays does not preclude strong focusing where wake gradients align. Fig. 8 presents sensitivity to incidence angle for near following conditions (θ_{rel} ranging from 5° to 20°) for T2 with T = 6 s waves. Strong sensitivity to incidence angle is observed and it is evident that strong convergence of

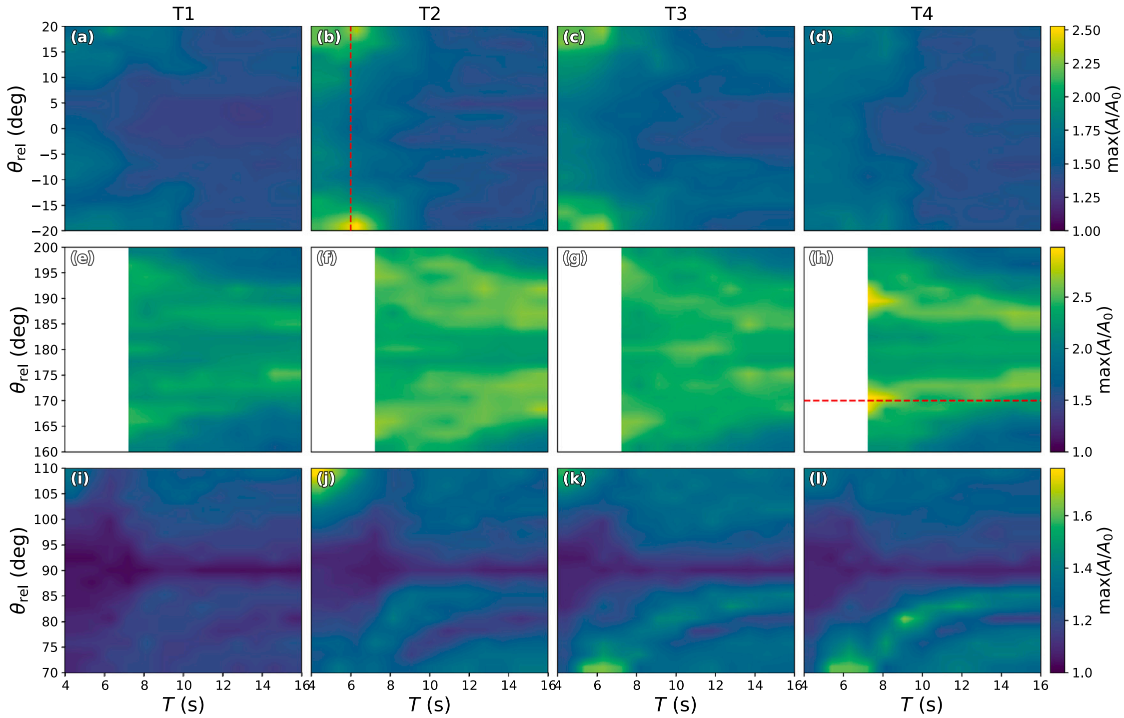

Fig. 9. Maximum normalised amplitude as a function of regular wave period and angle for different configurations (columns) and different nominal directions (rows). Shown for following waves for configurations T1–T4 (a)–(d), opposing waves for configurations T1–T4 (e)–(h), perpendicular waves for configurations T1–T4 (i)–(l). Red dashed lines represent cases assessed for location sensitivity in Figs. 10 and 11.

wave rays occurs for narrow angular ranges. The precise heading and location of these regions can be expected to vary with the array/wake structure, current velocity, turbine operating point etc.

Fig. 9 presents a summary of all regular wave results, summarised by the maximum amplification over the simulated domain for each turbine layout and for the range of wave periods and relative angles (for near-following, near-opposing, and near-oblique conditions). These results highlight the sensitivity of wave amplification to the range of parameters studied. For all cases large local amplifications are observed, exceeding 2.5× the incident amplitude for near-following conditions, around 3× the incident amplitude for near-opposing, and with more modest amplifications ($\approx 1.7 \times A_0$) predicted for near-perpendicular conditions. Generally larger peak local amplifications are observed for opposing conditions, which can be broadly explained by the fact that for a given wave period (in the fixed reference frame), the group velocities for opposing conditions will be lower, and therefore the same absolute changes to the current field cause larger changes to the wave properties. In the wave ray tracing model used here, there is therefore higher potential for strong wave ray convergence and associated large amplifications, representing refractive focusing.

It must be emphasised that the wave-ray tracing formulation relies on the WKB approximation, which inherently predicts infinitely sharp, singular peaks at refractive caustics. Consequently, the peak values of regular wave amplifications reported here (e.g. $A/A_0 \geq 3.0$) represent theoretical upper bounds, which can be considered conservative for design. As is explicitly addressed via a discussion of errors in Section 4.2 and phase-resolved comparisons in Section 4.3, physical wave diffraction allows energy to be smoothed out, which can be expected to broaden the spatial extent of the focusing regions whilst reducing the peak values of wave amplification.

We further explore how the locations of these large amplifications vary with both wave period and incidence angle, with implications for wave height amplification for realistic frequency and directional distributions as assessed in Sections 3.2 and 3.3. Here, we identify and plot regions where the amplitude ratio exceeds an amplification threshold chosen to be $A/A_0 > 1.6$ for a range of incidence angles (Fig. 10: demonstrated for T2, near-following waves with $T = 6$ s) and periods (Fig. 11: demonstrated for T4, near-opposing waves with $\theta_{rel} = 170°$). This value is intended to identify the regions in which clearly defined focusing events occur, without too much visual overlap, to aid interpretation. These correspond to the red dashed lines in Fig. 9.

It is evident from Fig. 10 that exceedance regions are most prominent only at larger $|\theta_{rel}|$ values, and that spatial locations of maxima shift systematically with incidence angle. This implies that directional spreading will smooth-out amplification effects, which is investigated further in Section 3.3.

The effect of wave period on the location of amplification regions is shown in Fig. 11. Similar trends are observed to the effect of heading but there are also notable differences. Firstly there are consistently regions over the threshold amplification across all periods. Secondly, peak locations are strongly correlated across T. Refraction does translate the focal regions spatially, but substantial overlaps persist across wave periods. As a result, for this scenario including realistic frequency spectra would only partially smooth the focusing effects. This is further explored in Section 3.2.

3.2. Unidirectional irregular waves

Results are presented for irregular wave conditions where, as detailed in Section 2.3, weighted amplification maps are used to represent irregular seas. Here we use JONSWAP spectra with different headings and peak periods (T_p), all with peak enhancement factor γ of 3.3. These are also computed for all 4 turbine layouts (T1–T4).

Fig. 12 illustrates sensitivity to configuration for irregular waves with $T_p = 10$ s, $\theta_{rel} = 190°$. Compared to Fig. 6, which is the equivalent for regular waves, smoothing effects are observed and peak amplifications are reduced from around $2.5A_0$ to $1.9A_0$. The location of peak amplifications also differs, and for irregular waves, the peak amplification location is in the negative y region (which was present for

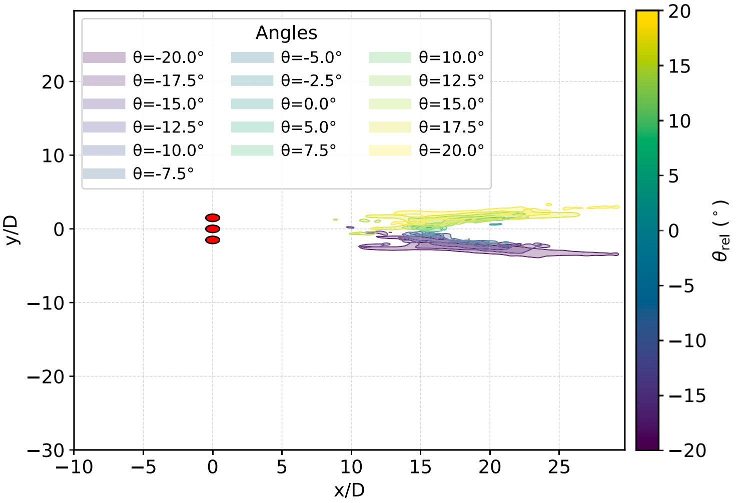

Fig. 10. Regions of high-amplitude overlaid for a fixed period (T = 6 s) and for configuration T2 as wave angle varies (indicated by a red line in Fig. 9). For each angle, the translucent patch shows where the amplitude ratio exceeds the absolute threshold $A/A_0 \geq 1.6$. Patch colour encodes the wave angle, and outlines mark the threshold contour. Turbine locations are shown as red markers.

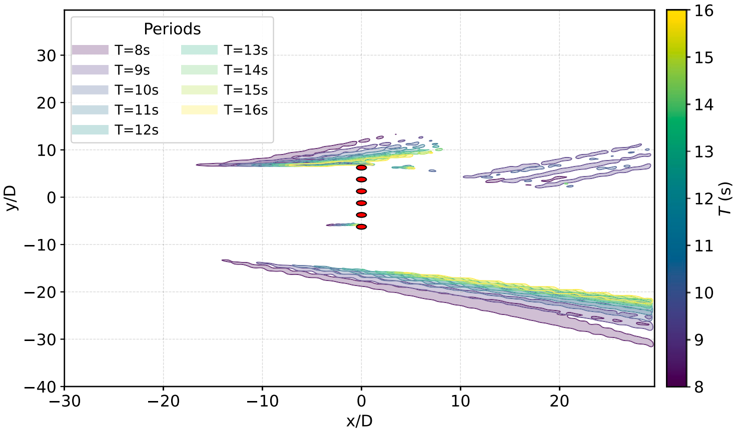

Fig. 11. Regions of high-amplitude overlaid for a fixed incident angle (θ_{rel} = 170°) and for configuration T4 as wave period varies (indicated by a red line in Fig. 9). For each period, the translucent patch shows where the amplitude ratio exceeds the absolute threshold $A/A_0 \geq 1.6$. Patch colour encodes the wave period, and outlines mark the threshold contour. Turbine locations are shown as red markers.

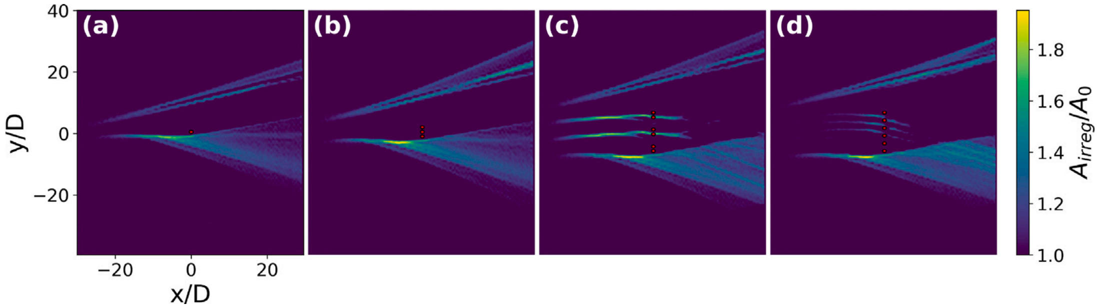

Fig. 12. Normalised irregular wave amplitude for different turbine configurations, for T_p = 10 s waves at 10 deg relative to opposing the mean current direction i.e. θ_{rel} = 190°. Shown for (a) T1, (b) T2, (c) T3, (d) T4. Turbine locations are shown as red circles.

regular waves but the location of peak amplification differs) compared with in the positive y region for regular waves. This demonstrates that some ray convergence zones exhibit greater sensitivity to period than others. It is interesting to note that the larger inter-array spacings between pairs of turbines for T3 have a considerable effect on the amplification fields.

Fig. 13 shows example sensitivity to peak wave period for T3 for opposing waves (θ_{rel} = 180°). Again, compared to the equivalent regular wave results (Fig. 7) smoothing effects are observed with peak amplifications reducing from around $2.5A_0$ to around $2A_0$. Similar sensitivity to peak period is also noted, where larger wave periods are less effected by refraction and hence wave ray curvature is lower. However, this does not appear to substantially reduce the maximum wave amplifications predicted.

Wave angle sensitivity shows similar behaviour. Fig. 14 presents fields for T2 at T_p = 8 s with near-following headings. Compared with

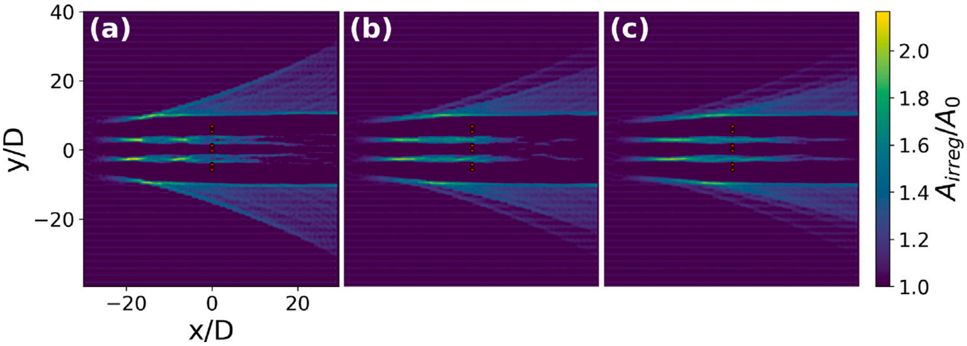

Fig. 13. Normalised irregular wave amplitude for different peak periods T_p over turbine configuration T3, for waves opposing the mean current direction i.e. $\theta_{rel} = 180°$. Shown for (a) $T_p = 8$ s, (b) $T_p = 10$ s, (c) $T_p = 12$ s. Turbine locations are shown as red circles.

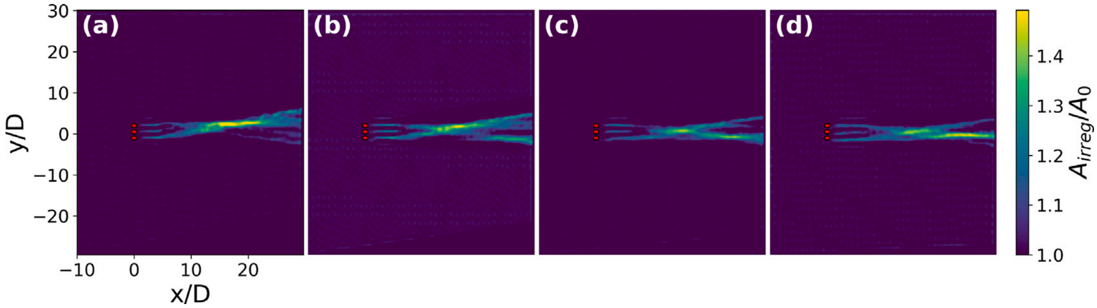

Fig. 14. Normalised irregular wave amplitude for different wave angles over turbine configuration T2, for $T_p = 8$ s waves close to following the mean current direction. Shown for (a) $\theta_{rel} = 20°$, (b) $\theta_{rel} = 15°$, (c) $\theta_{rel} = 10°$ (d) $\theta_{rel} = 5°$. Turbine locations are shown as red circles.

the regular wave counterparts (Fig. 8), the maps are smoothed yet retain sharp dependence on θ_{rel}; for this scenario, within the 5°–20° range, larger incidence angles produce the largest peaks for this array layout and wave spectrum.

Fig. 15 summarises peak amplification across turbine layout, peak wave period T_p, and wave incidence angle. The qualitative ordering of peak amplification is similar to the regular wave results (Fig. 9): opposing > oblique > following, with strong sensitivity to layout. For the same period and heading as regular waves the irregular waves reduce $\max(A/A_0)$ due to spectral smoothing. This is because neighbouring components refract by different amounts, lowering co-located peaks without eliminating focusing phenomena overall.

3.3. Directionally spread irregular waves

We finally consider directionally spread seas with Gaussian spreading of fixed standard deviation σ_θ about the mean heading $\overline{\theta_{rel}}$. We limit analysis to $\overline{\theta_{rel}}$ values of 0°, 180°, and 90° i.e. following, opposing and perpendicular. The other angular components simulated (±20° range from the mean directions) contribute to the weighted amplification fields as described in Section 2.3. To simulate directionally spread wave fields we use a frequency-independent Gaussian directional spreading function (see e.g. McAllister et al., 2024) and vary the standard deviation or directional spreading width σ_θ.

Fig. 16 shows example sensitivity to turbine configuration for directionally spread irregular waves with $T_p = 10$ s, mean direction $\overline{\theta_{rel}} = 180°$, and directional spreading width $\sigma_\theta = 5°$. The peak amplification shows further smoothing effects relative to both unidirectional irregular and regular wave conditions. There is also interesting sensitivity to the turbine configuration observed. For the single turbine wake (layout T1) local amplification is negligible ($\max(A/A_0) \approx 1$) whereas for the six turbine wakes (T3 and T4) peak amplification exceeds $1.4A_0$. For these layouts and condition, the effect of the array spacing is very pronounced: for T3 there is large focusing between the clustered pairs of turbines, yet for T4 there is clear focusing on both sides of each turbine. The smaller inter-turbine spacings for T2 result in no focusing between the three turbines.

Fig. 17 shows sensitivity to peak wave period for T3 for opposing directionally spread irregular waves ($\overline{\theta_{rel}} = 180°$) with $\sigma_\theta = 5°$. Compared to the equivalent regular and irregular unidirectional results (Figs. 7 and 13) smoothing effects are observed with peak amplifications reducing from around $2.5A_0$ for regular waves and $2A_0$ for irregular unidirectional to around $1.5A_0$ for directionally spread waves. Similar minor sensitivity to T_p is noted.

An example of sensitivity to directional spreading, σ_θ, is presented in Fig. 18 for T2 with $T_p = 8$ s. The smoothing effects of increasing directional spreading are evident, with peak amplifications reduced considerably for high values of directional spreading.

The peak amplifications for directionally spread sea states are summarised in Fig. 19 as a function of T_p, configuration, and directional spreading and compared to those for the equivalent unidirectional and regular waves. This plot thus summarises the smoothing effects of both frequency and directional bandwidth for normally incident wave conditions relative to the velocity field. The results are generally as would be expected: including frequency bandwidth reduces peak amplifications relative to regular waves, and increasing directional spreading further serves to reduce peak amplifications through spatial smoothing effects.

Assessing Fig. 19, somewhat unexpectedly it is found that the smoothing effects associated with directional spreading are not as large for following wave conditions as they are for opposing conditions. As noted when discussing Fig. 16 some opposing conditions essentially become completely smoothed out e.g. most T1 conditions with high directional spreading, which is not observed for any following cases. This highlights significant complexity in how wave components that undergo different refraction paths interact and cause spatial focusing.

Overall, it is clear that tidal turbine wakes have the potential to focus waves and substantially increase local amplifications. Such

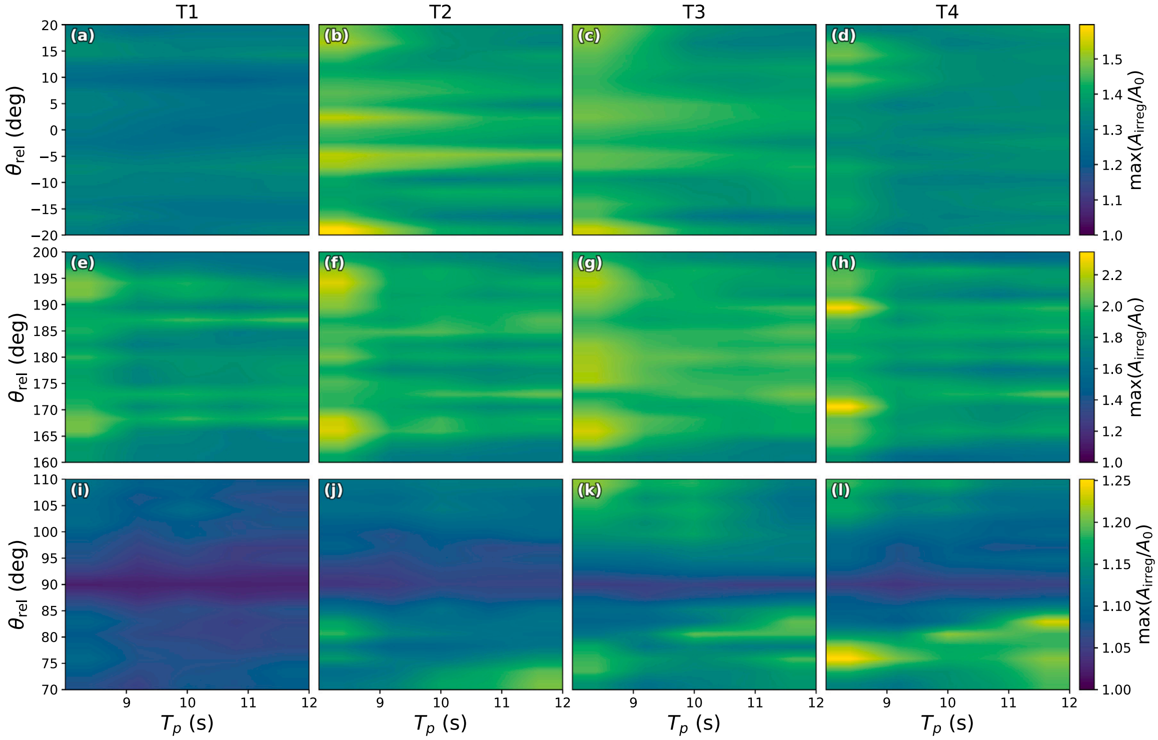

Fig. 15. Maximum normalised amplitude for irregular waves as a function of peak period and angle for different configurations (columns) and different nominal directions (rows). Shown for following waves for configurations T1–T4 (a)–(d), opposing waves for configurations T1–T4 (e)–(h), perpendicular waves for configurations T1–T4 (i)–(l).

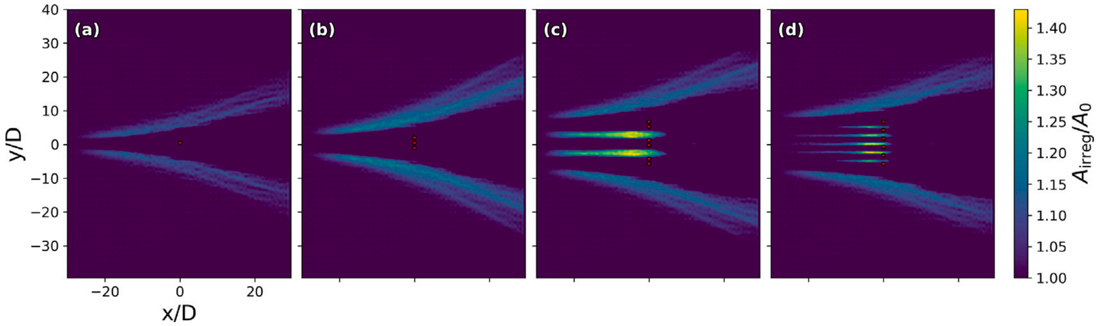

Fig. 16. Normalised irregular directionally spread wave amplitude for different turbine configurations, for $T_p = 10$ s waves with mean direction opposing the mean current direction i.e. $\overline{\theta_{rel}} = 180°$, and $\sigma_\theta = 5°$. Shown for (a) T1, (b) T2, (c) T3, (d) T4. Turbine locations are shown as red circles.

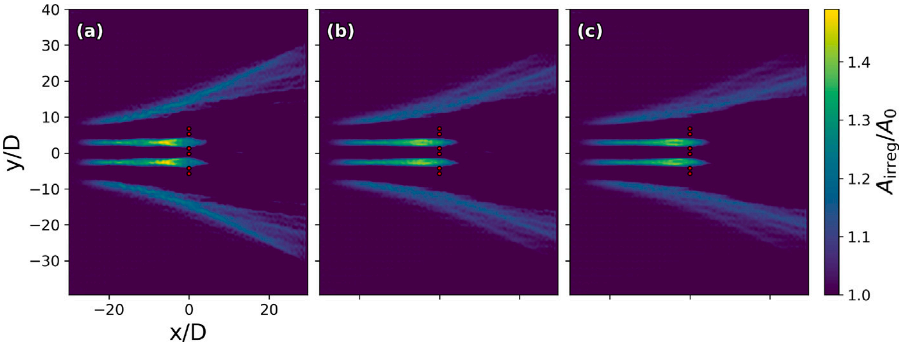

Fig. 17. Normalised irregular directionally spread wave amplitude for different peak periods T_p over turbine configuration T3, for waves with mean direction opposing the mean current direction i.e. $\overline{\theta_{rel}} = 180°$, and $\sigma_\theta = 5°$. Shown for (a) $T_p = 8$ s, (b) $T_p = 10$ s, (c) $T_p = 12$ s. Turbine locations are shown as red circles.

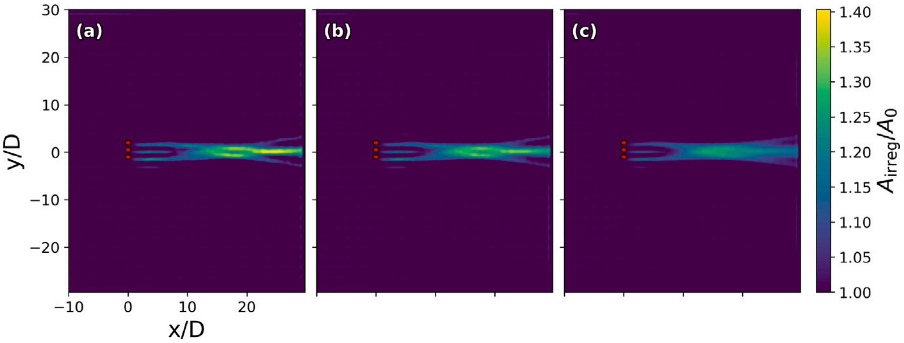

Fig. 18. Normalised irregular directionally spread wave amplitude for different directional spreading widths σ_θ over turbine configuration T2, for $T_p = 8$ s waves following the mean current direction i.e. $\overline{\theta_{rel}} = 0°$. Shown for (a) $\sigma_\theta = 2.5°$, (b) $\sigma_\theta = 5°$, (c) $\sigma_\theta = 10.0°$. Turbine locations are shown as red circles.

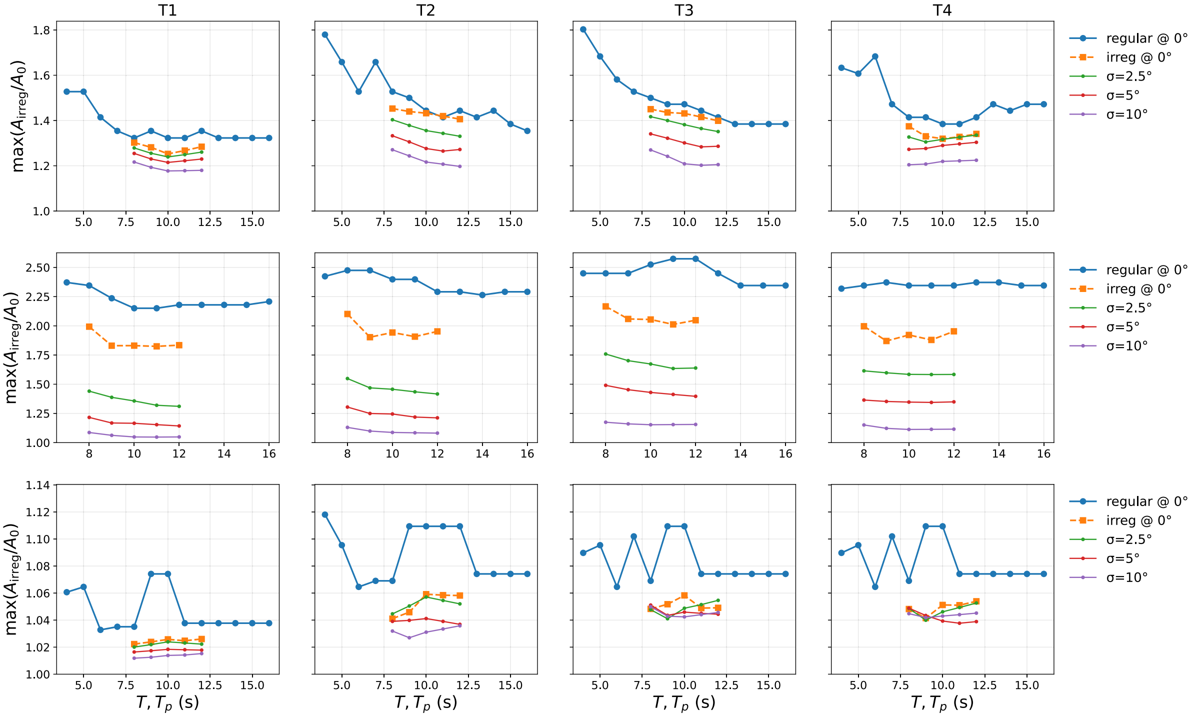

Fig. 19. Maximum normalised amplitude for directionally spread irregular waves as a function of peak period for different configurations (columns) and different nominal directions (rows). Shown for following waves for configurations T1–T4 (a)–(d), opposing waves for configurations T1–T4 (e)–(h), perpendicular waves for configurations T1–T4 (i)–(l). Results are shown for different values of directional spreading σ_θ and compared against both irregular unidirectional and regular wave peak amplification for normal incidence.

changes of wave conditions may affect turbine loading and/or the choice of turbine siting in arrays and should not be omitted from TST array design and operation considerations. The expected amplifications, however, are dependent on the frequency and directional bandwidth of the sea states, and therefore these aspects of ocean waves cannot be ignored. There have been several assumptions and simplifications made in this work which are discussed further in Section 4.

3.4. Spatial extent of wave amplification

While the peak amplification ratio $\max(A/A_0)$ serves as a useful metric for identifying the most extreme theoretical focusing conditions, structural array design ultimately requires an understanding of the spatial footprint of these hazards. Because the phase-averaged ray-tracing model does not explicitly simulate diffraction, energy at exact focal caustics will be over-predicted (as assessed further in Section 4.3). To provide a more robust contextualisation of the risk to TST arrays, we evaluate the total normalised area ($Area/D^2$) over which the local wave amplitude exceeds specific thresholds ($1.1A_0$, $1.3A_0$, and $1.5A_0$).

Fig. 20 summarises these threshold exceedance areas across all turbine configurations, wave periods, and sea states for normally incident waves (following and opposing). We omit perpendicular results due to the low amplifications evident in Fig. 19.

Assessing Fig. 20, it is evident that the spatial footprint of wave amplification under opposing flow conditions is an order of magnitude larger than under following conditions. For example, the area experiencing at least a 10% amplification ($A/A_0 \geq 1.1$) routinely exceeds $800D^2$ for opposing regular waves, compared to less than $150D^2$ for following waves. This underscores opposing wave–current alignments as the primary driver of persistent, wide-area farm loading variability.

Secondly, the introduction of realistic spectral characteristics dramatically reduces the spatial footprint of extreme focusing in the majority of cases. For regular waves, the area exceeding $1.5A_0$ (dotted blue lines) remains substantial across all configurations. However, the

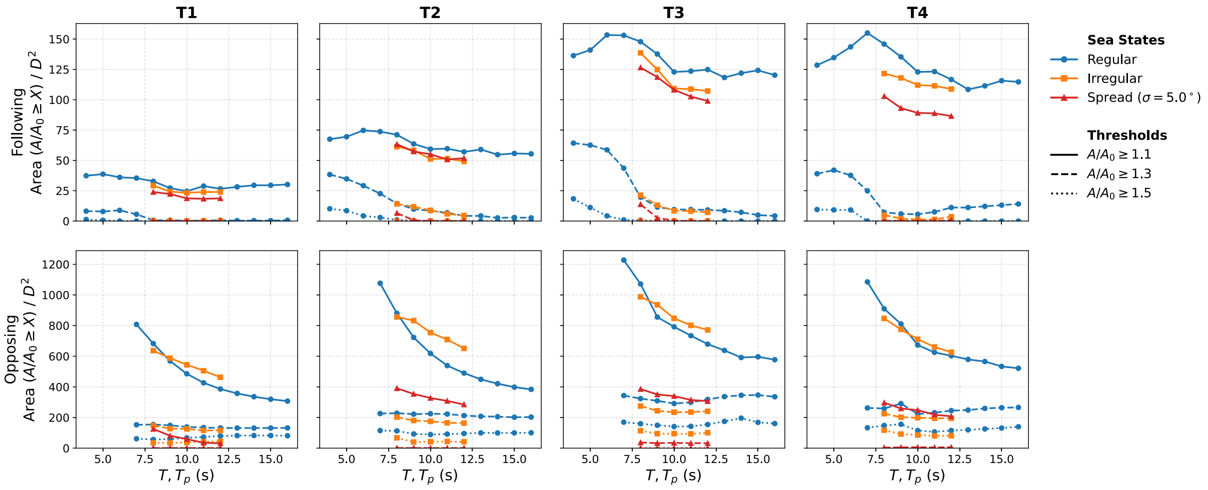

Fig. 20. Normalised spatial area ($Area/D^2$) exceeding amplification thresholds A/A_0 of 1.1, 1.3, and 1.5 across varying wave periods. Results are shown for regular, irregular unidirectional, and directionally spread ($\sigma = 5°$) sea states under both following and opposing normal incidence.

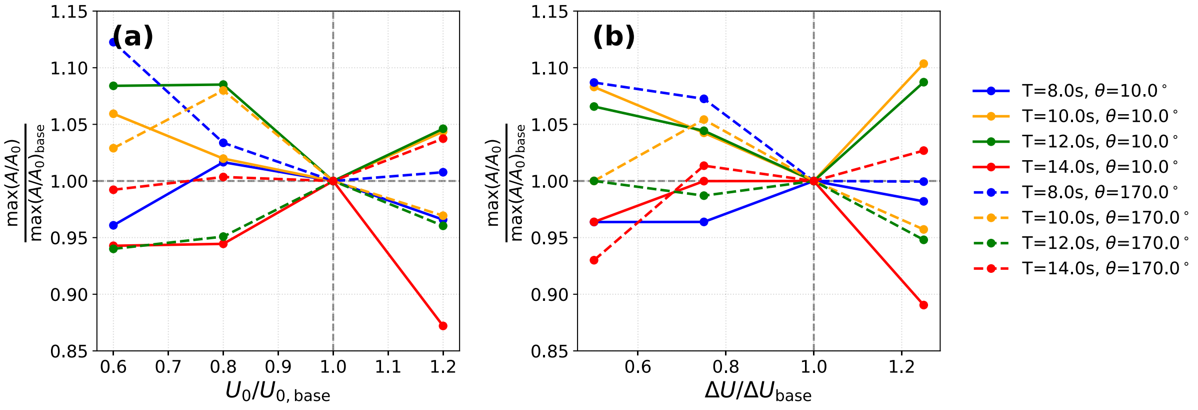

Fig. 21. Sensitivity of maximum wave amplification to physical flow parameters, normalised against a baseline condition. (a) Effect of varying freestream speed U_0 relative to the baseline $U_{0,\text{base}} = 2.5$ m/s. (b) Effect of scaling the wake velocity deficit ΔU relative to the baseline empirical deficit ΔU_{base}. For each wave condition, the peak amplification ratio (A/A_0) is normalised by the peak amplification observed at the baseline state ($U_0 = 2.5$ m/s, Deficit Multiplier = 1.0). For context, these absolute baseline peaks range from 1.3 to 1.5 for near-following waves, and from 1.85 to 2.05 for near-opposing waves. Solid lines indicate near-following waves ($\theta = 10°$), while dashed lines indicate near-opposing waves ($\theta = 170°$) across a range of regular wave periods (T = 8–14 s).

introduction of frequency bandwidth (irregular waves, orange lines) noticeably suppresses this extreme area. Furthermore, when directional spreading is applied (red lines), the area exceeding $1.5A_0$ collapses to virtually zero across the entire parameter space. Crucially, however, these spectral smoothing effects do not simply remove the amplified wave energy; rather, it redistributes it. As a result, for lower and moderate amplification thresholds (e.g. $A/A_0 \geq 1.1$), introducing frequency bandwidth can sometimes increase the total affected area relative to regular waves. Because the sharp refractive focusing of individual frequency components occur at slightly different spatial locations (see Fig. 11), their superposition in an irregular sea smears the concentrated energy over a broader geographic footprint.

While directional spreading ultimately reduces both the peaks and the broad footprints, the area of moderate amplification ($1.1A_0$) remains remarkably persistent across all configurations. Spreading effectively eliminates the sharp, extreme peaks, yet the broader refractive focusing still occurs. This demonstrates that while TST arrays are unlikely to subject down-wave devices to sustained extreme wave loads ($>1.5A_0$) in highly directionally spread realistic ocean conditions, persistent moderate amplification ($1.1A_0$ to $1.3A_0$) is practically unavoidable and will span large areas of the turbine farm, necessitating careful consideration during array micro-siting and fatigue life assessment.

4. Discussion

This section assesses sensitivity to the flow conditions (Section 4.1), the significance of key modelling assumptions (Section 4.2), a like-for-like comparison to a phase-resolved Boussinesq model (Section 4.3) for waves over a jet, and areas for future work (Section 4.4).

4.1. Sensitivity to flow conditions

The refractive strength of the wake is governed by the background velocity magnitude (U_0) and the velocity deficit (ΔU). To assess the robustness of the predicted focusing, a parametric sweep was conducted across these variables. While the resulting trends (below) exhibit some non-monotonicity due to the spatial shifting of focal peaks and complexity of how ray convergence and focusing occurs, the presence of significant wave amplification remains a persistent feature across all tested configurations. As shown in Fig. 21, despite varying the freestream velocity by up to ±40% and the wake deficit by up to ±50%, the maximum amplification ratio remarkably remains within roughly ±10 – 15% of the baseline value for almost all conditions.

4.1.1. Influence of background velocity (U_0)

The sensitivity of wave amplification to the background current speed U_0 is shown in Fig. 21a. For both the near-following ($\theta_{rel} = 10°$)

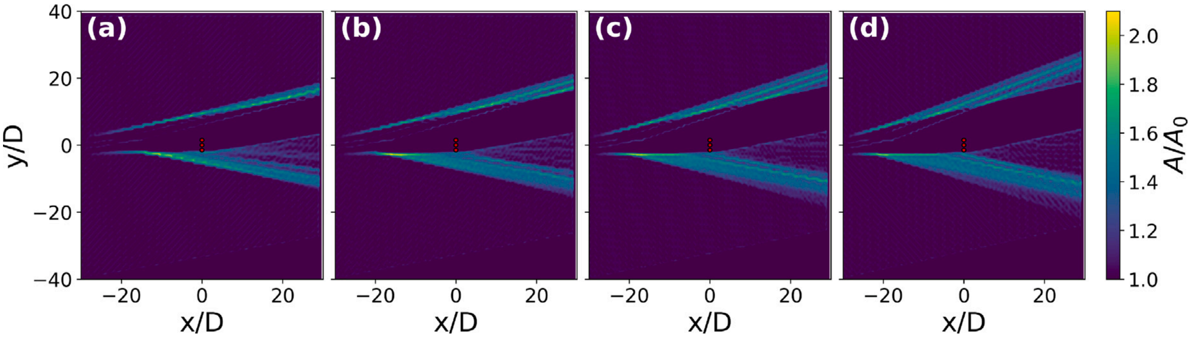

Fig. 22. Spatial maps of wave amplification (A/A_0) demonstrating the effect of varying the background velocity U_0 for a representative near-opposing case (T = 10 s, θ_{rel} = 170°). Panels show U_0 values of (a) 1.5, (b) 2.0, (c) 2.5, and (d) 3.0 m/s.

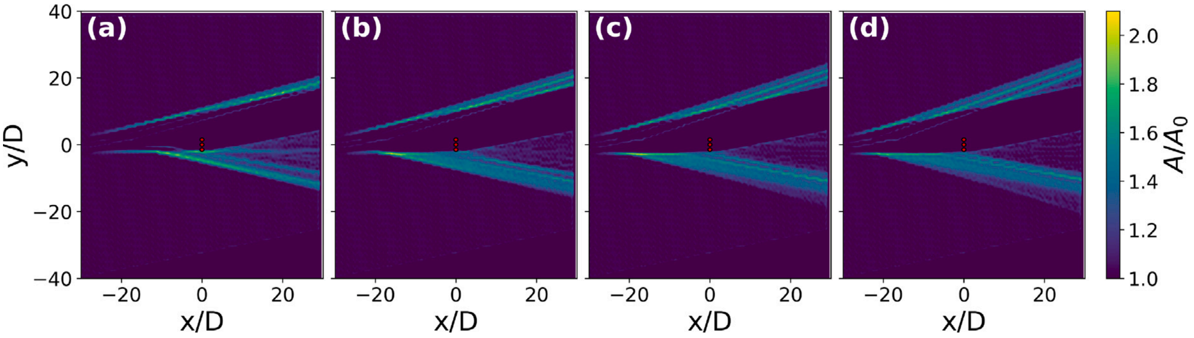

Fig. 23. Spatial maps of wave amplification (A/A_0) demonstrating the effect of scaling the wake velocity deficit for a representative near-opposing case (T = 10 s, θ_{rel} = 170°). Panels show deficit multipliers of (a) 0.5, (b) 0.75, (c) 1.0, and (d) 1.25.

and near-opposing (θ_{rel} = 170°) wave–current configurations, the peak A/A_0 values consistently exceed 1.35 across the range $1.5 \leq U_0 \leq 3.0$ m/s for near-following conditions, and are above A/A_0 values of 1.85 across all U_0 values for near-opposing cases.

In these near-opposing cases (T = 8.0 s), amplification remains particularly high, reaching values of around 2.05. This indicates that the refractive focusing effect is a fundamental characteristic of the shear that persists across all flow speeds. The persistence of these peaks suggests that the risk of localised extreme wave loading from refractive focusing over wakes is not restricted to a narrow operational velocity but is a broader concern for tidal array design.

To visualise this, Fig. 22 presents spatial amplification fields for a representative near-opposing case (T = 10 s, θ_{rel} = 170°). As U_0 increases from 1.5 to 3.0 m/s (panels a to d), the primary features of the wake-induced refraction remain consistent, despite having a larger lateral extent for smaller U_0 values where the refractive effects are smaller. While the focal intensity and exact coordinates shift with the current speed, the overarching structure of the converging rays is conserved, highlighting a surprising insensitivity to quite large changes to the flow speed.

4.1.2. Influence of velocity deficit

The velocity deficit acts as the primary driver of the focusing mechanism. In Fig. 21b, we scale the velocity deficit from the turbine wake model by a constant multiplier (the ‘velocity deficit multiplier’). Values are assessed between 0.5 to 1.25 to represent different turbine thrust. The relationship between the velocity deficit and the peak amplifications A/A_0 is complex and, somewhat counter-intuitively, does not clearly increase with the velocity deficit. This highlights that there are complexities associated with which flow field and wave condition combinations provide maximal convergence of rays and hence localised focusing.

The example spatial maps provided in Fig. 23 (for T = 10 s, θ_{rel} = 170°) adds context. Scaling the velocity deficit alters the refractive capacity. As the deficit multiplier varies, the focal point translates longitudinally along the wake centreline and the lateral extent contracts or expands.

The persistence of these peaks across varying deficit strengths (from 0.5 to 1.25 times the baseline) suggests that the broad wave–current focusing mechanisms observed are persistent, and somewhat robust to uncertainties in the exact wake decay profile, provided that a significant enough lateral shear is present (evidently present for all cases tested here).

4.2. Estimates of modelling errors

In using the wave ray tracing model for this study, we are assuming that refractive focusing effects are dominant. This is strongly supported by earlier preliminary works (Olczak, 2016); however, there still exist several limitations of this approach due to a variety of assumptions and model limitations. In Section 4.2.1 we assess the potential errors associated with omitting reflections from the rapidly changing current in the wake along with omitting conservation of wave action along wave rays. In Section 4.2.2 we estimate the maximum expected errors due to omitting wave-induced power modification from waves interacting with the turbine.

While the sharp velocity gradients immediately behind the rotors stretch the limits of the WKB approximation (slow spatial variation relative to wavelength), the primary convergence of wave energy observed in the most extreme focusing cases, with waves opposing the current, is driven by interactions with the far wake. In this region, the velocity deficit has decayed and spread, presenting smoother gradients that better match the WKB assumptions. The physical robustness of the broad focal regions is also supported by comparison to phase-resolved Boussinesq simulations presented in Section 4.3.

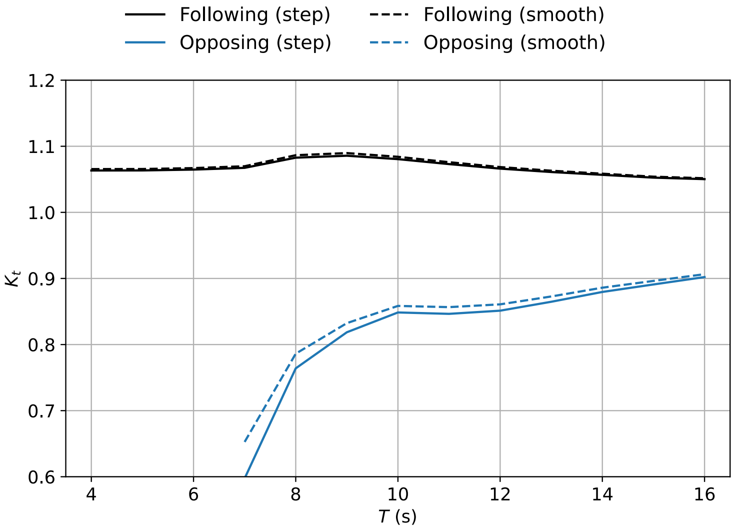

Fig. 24. Predicted transmission coefficients local to the maximum velocity deficit for following and opposing waves using approximations for a sharp (Eq. (21)) and smooth (Eq. (22)) velocity transition considering location of maximum effective velocity deficit.

4.2.1. *Reflection and transmission errors*

As mentioned, the wave ray tracing assumptions do not strictly apply over the sharp wake transitions due to the associated rapid changes in the wavenumber over small spatial scales. It is evident, however, that the sharp wake transitions are smoothed out when considered in a depth-averaged sense (Fig. 3(d)). To estimate the maximum amplitude error introduced by ray-tracing assumptions, we consider two limiting cases for rays that cross the wake centreline: (i) an idealised sharp velocity step between the freestream and the wake centre, and (ii) a smooth, no-reflection limit. The details of the calculations are presented in Appendix B.1, where we calculate the expected modification to the transmission coefficient K_t: incident conditions are defined by the freestream velocity U_0, while transmitted conditions correspond to the location of maximum effective velocity deficit (see Eq. (11)). The results are presented in Fig. 24, where values of K_t greater and smaller than unity indicate amplification and attenuation, respectively. These effects are not captured using the wave ray tracing model. As expected, the step assumption gives smaller K_t values than the smooth WKB assumption. There is a value of the transmission coefficient above unity for the following wave conditions which corresponds to an increase in the amplitude due to a reduction in the velocity (and therefore of the absolute group velocity $c_{g,abs}$) in the wake. The fact that the two approximations give very similar estimated errors shows that the dominant discrepancy is from the amplitude change from the conservation of wave action as opposed to any potential reflections from the interface (which can be interpreted as the difference between the lines).

The results in Fig. 24 show that the largest deviations occur for low period opposing waves for which group velocities are small and the change in the flow field induces the largest change to the waves, as expected. For most other conditions, differences are moderate with maximum possible expected amplitude errors of around 5%–10% which is considerably less than the amplifications observed, and this supports the use of the wave ray tracing model for qualitative and comparative analyses. Importantly, it is to be noted that because the error is attributed largely due to local amplitude modification due to the presence of the current and not reflections, if the amplification region of interest is not within the wake itself, then the errors will be much reduced. As turbines in arrays are designed to be in locations not in the centre of other wakes, and close to the freestream velocity for power generation considerations, the actual amplification errors could be negligible.

It is worth noting that in Fig. 24 there is a contrast between the effective velocity change sampled by the waves and the resulting amplitude error. The maximum effective deficit $\max(\Delta U_e)/U_0$ tends to increase with period because longer waves (larger ϵL in Eq. (11)) integrate over more of the vertical structure of the wake and therefore 'experience' a larger deficit. However, the largest amplitude deviations do not occur at the largest T. For opposing seas the peak error is at shorter periods. This is because as T decreases the group velocity c_g decreases significantly and therefore the waves are more affected by the changes to the current, even if the effective change in the current is smaller. In following seas the trend is more balanced: low period waves sample a smaller ΔU_e (limited vertical reach) but sensitivity is reduced for very long waves which occur for high period following conditions.

4.2.2. *Wave power change*

The waves can lose or gain power, and therefore reduce or increase in amplitude locally, due to doing work on (or receiving work from) the turbine. We develop a simplified model to estimate the magnitude of this effect with the full derivation given in Appendix B.2.

As detailed in Appendix B.2, the sign of the mean exchange is set by U_e: following ($U_e > 0$) yields damping (power loss from the waves), while opposing ($U_e < 0$) can produce a small amplification (power gain to the waves) by transferring energy from the mean current to the waves. It is interesting to note that despite power increasing for waves opposing the current (and direction of rotor thrust), that the mean power available to the turbine is also expected to increase (at least under simplified models e.g. Draycott et al., 2019b), highlighting that an increase in energy is transferred from the mean flow to both the turbine and the wave field under opposing conditions. This is consistent with earlier works showing how currents can do work on waves and vice versa (Longuet-Higgins and Stewart, 1962; Smith, 2006).

The results of this analysis are shown for both opposing and following conditions in Fig. 25 as a function of wave period, using $U_e = \pm 2.5$ m/s. The values presented represent the largest local changes to power and wave amplitude due to interaction with the turbine for collinear conditions. The largest changes in both power and amplitude are observed, in general, for larger periods due to the lower wavenumbers and associated larger velocities further down in the water column where the rotors are located. Overall, a peak change in amplitude of around 3% indicates this is not a large source of error owing to the simplified wave ray tracing model. This effect may, however, accumulate over many rows of turbines and so could become appreciable at farm scale.

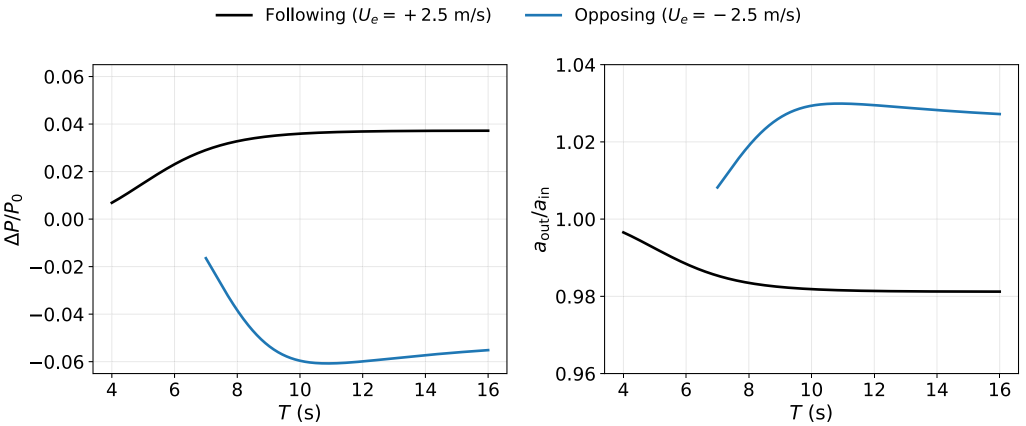

Fig. 25. Signed change in wave power local to the turbine due to work exchange with the turbine, and associated amplitude change, assuming collinear wave–current–turbine interactions. Positive $\Delta P/P_0$ denotes damping (following), negative denotes slight amplification (opposing).

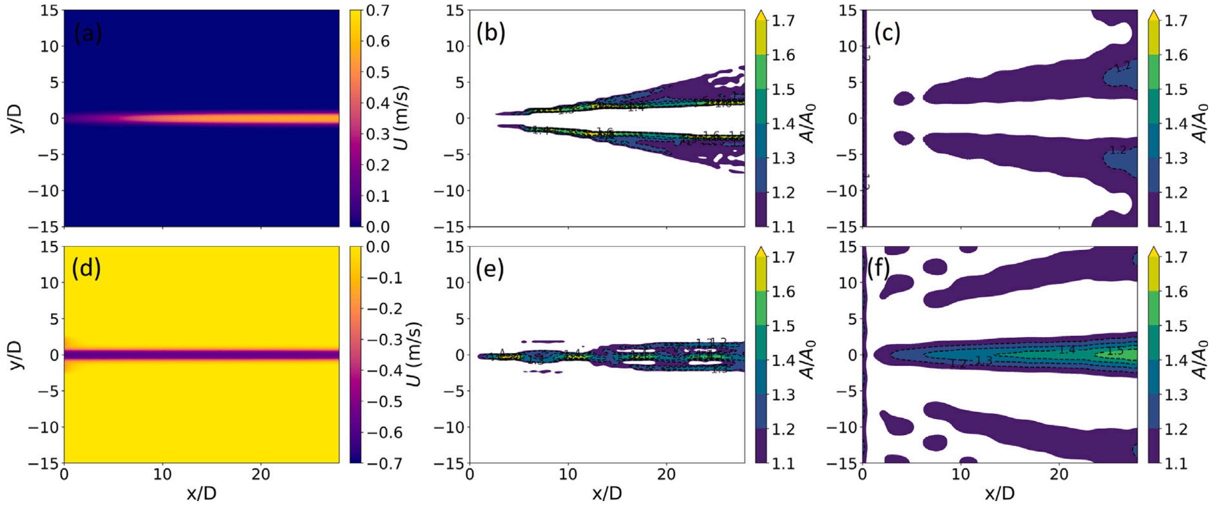

Fig. 26. Comparison of the initial streamwise velocity field (U) and resulting spatial wave amplification (A/A_0) between the phase-averaged wave-ray tracing model and the phase-resolved FUNWAVE-TVD model for $T = 8$ s regular waves. Top row represents following conditions ($\theta_{\text{rel}} = 0°$): (a) initial velocity field U, (b) wave-ray tracing A/A_0, and (c) FUNWAVE-TVD A/A_0. Bottom row represents opposing conditions ($\theta_{\text{rel}} = 0°$): (d) initial velocity field U, (e) wave-ray tracing A/A_0, and (f) FUNWAVE-TVD A/A_0. In all simulations wave propagate from left to right.

4.3. Comparison to phase-resolved simulations

To validate the fundamental refractive focusing mechanisms predicted by the wave-ray tracing approach, a like-for-like comparison to the phase-resolved Boussinesq wave model, FUNWAVE-TVD (Shi et al., 2012), was conducted. This allows for an assessment of the focusing phenomena with higher-fidelity physics that inherently include wave phase, wave diffraction, scattering, and the conservation of wave action.

A single idealised jet (representative of the scale and velocity shear developed by a turbine wake) is presented for regular waves with $T = 8$ s under strictly collinear following and opposing conditions ($\theta_{\text{rel}} = 0°$). In the FUNWAVE-TVD simulations, an initial Gaussian velocity deficit with a large ΔU (see Fig. 26a,d) is prescribed and allowed to dynamically evolve and become steady. Once the jet is established, waves are introduced via an internal wavemaker. To ensure a consistent baseline comparison, a 'hot-start' approach is used. The 'steady-state' velocity field from FUNWAVE at the exact moment of wave injection is extracted and used as the static background effective velocity field (U_e) for the corresponding wave-ray tracing simulation.

Despite this alignment of the initial conditions, several fundamental modelling differences remain. Most notably, the jet continues to dynamically evolve and advect in the FUNWAVE model as the waves propagate through the domain, whereas it remains entirely static in the ray-tracing model. This is expected to smooth out persistent focusing effects in the FUNWAVE model as the magnitude and location of velocity gradients change over time. Furthermore, FUNWAVE explicitly models diffraction and the conservation of wave action flux across the velocity gradients, phenomena which are absent in the simplified ray tracing model, as discussed above in Section 4.2. Finally, the phase-resolved simulations are subject to numerical boundaries, such as wavemaker interactions within the jet and the performance of the absorbing sponge layers (implemented on all sides). To minimise the effect of incomplete absorption, we analyse a time (and spatial) window of (exactly) 5 wave periods (100 s to 140 s) for which incident waves are fully developed throughout the domain but boundary reflections are not yet present. Within this steady-state window, the local wave amplitude field is calculated from the temporal variance (Var) of the surface elevation, $A(x,y) = \sqrt{2\text{Var}(\eta)}$, and is subsequently normalised by the incident amplitude sampled from an undisturbed region near the wavemaker.

The initial jets used for the 'hot start', and the resulting spatial amplification fields for both models are presented in Fig. 26. A direct comparison reveals strong agreement regarding the locations of maxima, whilst also clearly highlighting the expected differences due to the varying physical fidelity.

For the following wave case shown in Fig. 26a–c, the wave-ray tracing model predicts a distinct “shadow zone” behind the wake where rays diverge, resulting in a region of reduced wave height ($A/A_0 < 1$). The FUNWAVE-TVD results confirm this physical mechanism, capturing a comparable region of amplitude reduction along the centreline (noting the jet is also advecting left to right over the duration of the run). Focusing is apparent in both models either side of this reduced amplitude region, yet is considerably higher in the wave ray tracing model than the Boussinesq model: wave ray tracing outputs predict nearly $1.7A_0$ when binned over $0.5D$, compared with $1.3A_0$ for the FUNWAVE outputs.

For the opposing wave case (Fig. 26d–f), the ray-tracing model predicts extremely localised focusing along the wake centreline, driving intense and physically unrealistic local peaks. In contrast, FUNWAVE captures the exact same refractive focusing mechanism, but physically resolves it. Diffraction allows wave energy to spread out from these focal peak, reducing the absolute maximum amplitude from theoretical infinity ($1.8A_0$ when binned over $0.5D$) to approximately $1.7A_0$, but with amplification over a larger area. There is notably closer agreement in the magnitude of peak amplification for the opposing jet than the following jet, which is speculated to be at least partially due to the stable opposing jet over this region and timeframe. In this simulation, the jet is moving from right to left and we do not analyse the far right domain (through which the jet ‘disappears’ during the simulation) due to windowing the domain and time-series to avoid reflections, and as such the jet is very consistent in both simulations over the region of interest, and the two models are more comparable. Overall, the large amplifications that are observed for the opposing jet in both models, highlight that the large amplifications predicted can be physically realistic, yet the exact locations and amplitudes can differ from those predicted from wave ray tracing.

4.4. Future work

The preliminary phase-resolved comparison presented in Section 4.3 supports the core finding of this study: tidal turbine wakes act as persistent refractive lenses that can significantly amplify local wave conditions. This analysis also highlights limitations of the assumptions inherent to the wave ray tracing approach. As estimated in Section 4.2, the omission of wave action conservation and, importantly, diffraction leads to an inherent over-prediction of peak amplifications at focal positions, yet can under-predict the spatial extent of the affected regions (as evident in Fig. 26e,f).

Consequently, while wave-ray tracing serves as a highly efficient and practical tool for evaluating massive parameter spaces and arbitrary stationary background flows (which would be intractable with other modelling approaches), the absolute peak values of amplification should be treated with caution. Rather than viewing phase-resolved Boussinesq or fully coupled wave–current models solely as tools to quantify these limitations for simplified cases, further exploration of a hybrid approach would be valuable. By running high-fidelity models over a targeted subset of the wider parameter space (with comparable velocity fields), it may be possible to reanalyse (or tune) the fast ray-tracing outputs. Such a mapping, potentially leveraging machine learning trained on similar wake velocity deficits and spatial gradients, could mitigate unphysical local maxima while accurately broadening the focal regions.

Furthermore, as demonstrated in Section 3.4, realistic ocean conditions (frequency and directional bandwidth) also fundamentally smooth and redistribute energy spatially. Another avenue for future research will be determining the relative balance of these aspects, isolating how much reduction in peak amplification is driven by smoothing from physical diffraction versus smoothing from sea-state spreading, particularly when the regions of influence overlap, and determining how to appropriately parameterise both effects in rapid assessment tools.

In addition to the modelling errors noted above, there are several other assumptions and simplifications made such as assuming a one way coupling (even though waves are known to modify jet structures Lu et al., 2011 and enhance vertical mixing and wake recovery Ouro et al., 2024), omitting induction effects from the turbine, and assuming a flat bed and uniform incident flow field.

This preliminary work thus motivates several further topics for investigation. Future studies employing CFD and laboratory experiments are recommended to improve on these preliminary estimates and findings and extend analysis to more realistic conditions and turbine representations incorporating e.g. natural spatial variability, turbulence, and bathymetry variation. Such studies should, however, consider the importance of frequency and directional bandwidth effects to avoid over-estimating amplifications.

While the sensitivity analyses in Section 4.1 demonstrate how variations in freestream velocity and wake deficit dictate the magnitude and location of wave amplification, this preliminary study certainly does not explore the full parametric space, and the relationships are shown to be complex. Future work should expand this to capture variations in flow speed and turbine thrust over a full tidal cycle, assessing a wider array of farm designs and operating strategies. Because bathymetric gradients can act as additional refractive lenses (Halsne and Li, 2025), coupling site-specific bathymetry with these array-scale wake models is a critical next step to accurately predict wave focusing and subsequent device-specific fatigue loading for planned field-scale deployments.

In addition to the modelling errors noted above, there are several other assumptions and simplifications made such as assuming a one way coupling (even though waves are known to modify jet structures (Lu et al., 2011) and enhance vertical mixing and wake recovery (Ouro et al., 2024)), omitting induction effects from the turbine, and assuming a flat bed and uniform incident flow field.

This preliminary work thus motivates several further topics for investigation. Future studies employing CFD and laboratory experiments are recommended to improve on these preliminary estimates and findings and extend analysis to more realistic conditions and turbine representations incorporating e.g. natural spatial variability, turbulence, and bathymetry variation. These future studies should, however, consider the importance of frequency and directional bandwidth effects to avoid over-estimating amplifications.

In addition to the implementation of more realistic modelling, there are several potential avenues of exploration with simplified models as presented here. While the sensitivity analyses in Section 4.1 demonstrate how variations in freestream velocity and wake deficit dictate the magnitude and location of wave amplification, this preliminary study certainly does not explore the full parametric space, and the relationships are shown to be complex. Future work should expand this to capture variations in flow speed and turbine thrust over a full tidal cycle, assessing a wider array of farm designs and operating strategies. Because bathymetric gradients can act as additional refractive lenses (Halsne and Li, 2025), coupling site-specific bathymetry with these array-scale wake models is a critical next step to accurately predict wave focusing and subsequent device-specific fatigue loading for planned field-scale deployments.

5. Conclusions

The spatially varying steady velocity field developed by multiple tidal turbine wakes has been shown to act as refractive lenses for surface gravity waves. This results in wave amplification in regular waves, and in realistic unidirectional and directionally spread seas that should be further considered for turbine and array design. Using wave-ray tracing on depth-integrated effective currents derived from an idealised three-zone turbine wake, wave amplification in the vicinity of four different turbine layouts are estimated across broad ranges of both wave period and wave heading. For regular waves, narrow bands of focusing form along the sides of the wakes with local peaks for near-following conditions exceeding $2.5A_0$; near-opposing close to $3A_0$, whereas near-perpendicular incidence angles produce weaker, yet still important, peaks up to around $1.7A_0$. The precise location and strength of the amplification depend on array layout, wave period and small changes in incidence angle: longer waves refract less yet can still generate strong hotspots where gradients align, and mild misalignment can change local behaviour from ray convergence (amplification) to ray dispersion (reduction). Preliminary comparisons with a phase-resolved Boussinesq model for waves over a jet demonstrates that while the spatial footprints of these focal zones are broadly robust, physical wave diffraction disperses energy and limits the absolute maximum amplitudes experienced in reality, whilst simultaneously broadening the amplification regions.

Introducing spectral realism (frequency bandwidth) smooths, but does not remove, the high amplification regions. Unidirectional irregular seas reduce peaks by around 30% for representative cases (still with peak amplification exceeding $2.2A_0$), and moderate values of directional spreading further limits amplification to around $1.75A_0$. Large values of directional spreading reduced amplifications to $1.35A_0$. The arrangement of rotors, and thus wakes, is shown to have a significant impact on focusing behaviour: paired turbines appear to encourage inter-pair focusing, whereas closely packed turbines can suppress inter-turbine focusing amplification hotspots entirely. Opposing seas generally give the largest local amplifications because reduced group velocities increase the relative effect of the current on the waves including, importantly, refraction. Interestingly, it is found that sufficiently large directional spreading results in negligible regions of amplification for the single turbine wake.

To estimate the impact of the primary assumptions employed in the simplified wave-ray tracing approach, theoretical transmission errors were computed for both sharp and smooth velocity transitions. This analysis indicates amplitude deviations (due to omitted conservation of wave action flux) of roughly 5%–10% for most cases. Larger discrepancies are only present for short-period opposing waves where up to 40% errors are expected in the wake core for conditions close to wave blocking. In addition, comparative validation against a phase-resolved Boussinesq model (FUNWAVE-TVD) demonstrated that while the omission of diffraction in the ray-tracing model leads to localised over-predictions of absolute peak amplitudes, and simultaneously an under-prediction of the affected areas, although the locations of these focusing regions are predicted correctly. Furthermore, parametric sensitivity analyses confirm that this wave–current focusing is a fundamentally robust feature of the flow shear; despite variations in freestream velocity and wake deficit of up to ±40%, relative peak amplifications remain remarkably stable (within roughly $\pm 10-15\%$ of baseline values). Taken together alongside estimates of wave power variation (expected to be $\approx 3\%$), these findings support the present framework as a practical, conservative (in terms of amplification levels) initial screening tool for scoping array-scale wave–current interactions and informing turbine micro-siting prior to computationally expensive high-fidelity modelling.

Overall, this paper demonstrates that wake-induced refraction can substantially modify wave amplitudes at scales of relevance to rotor loading, even in realistic, irregular and directionally spread seas. Array siting and operations should therefore consider the effect of lateral spacing, clustering and staggering on expected wave conditions to avoid persistent focusing locations in regions where turbines will be (are) installed. Future work should validate and refine these predictions using high-fidelity numerical models and targeted laboratory or field measurements with real turbine models and associated wakes, incorporating site-specific bathymetry and background shear, and explore control strategies that exploit opportunities for wave defocusing whilst also maintaining tidal turbine farm performance. Ultimately, the computational efficiency of the ray-tracing approach makes it an ideal foundation for future hybrid approaches. By coupling these rapid tools with targeted phase-resolved simulations to inform corrections accounting for spatial smoothing from diffraction effects, it may become possible to accurately and rapidly predict device-specific fatigue loading across vast parametric (and physical) spaces for planned field-scale deployments.

CRediT authorship contribution statement

Samuel Draycott: Writing – original draft, Visualization, Software, Methodology, Investigation, Formal analysis, Conceptualization. **Hannah Mullings:** Writing – review & editing. **Pablo Ouro:** Writing – review & editing. **Peter Stansby:** Writing – review & editing, Methodology. **Tim Stallard:** Writing – review & editing, Methodology.

Declaration of competing interest

The authors declare the following financial interests/personal relationships which may be considered as potential competing interests: Tim Stallard reports financial support was provided by Engineering and Physical Sciences Research Council. If there are other authors, they declare that they have no known competing financial interests or personal relationships that could have appeared to influence the work reported in this paper.

Acknowledgements

The authors acknowledge the SuperGen ORE Impact Hub [EP/Y016297/1] for supporting this work. The authors are extremely thankful to the authors of the Ocean wave tracing v.1 package for releasing this as open-source (Halsne et al., 2023): https://doi.org/10.5281/zenodo.7602540. This was instrumental in both the motivation and the practical implementation of this work. The authors would also like to thank the authors of the FUNWAVE-TVD code used for phase-resolved validation.

Appendix A. Numerical sensitivity and convergence

To ensure that the wave-ray tracing results presented in this study are independent of the chosen numerical discretisation, a systematic sensitivity study was performed. The model was tested against three primary parameters: the initial ray seeding density at the upwave boundary (N_{rays}), the spatial grid resolution of the underlying velocity field (N_{grid}), and the spatial averaging bin size (B) used to calculate wave density. As shown in Fig. 27, results are expected to be independent of N_{rays} and N_{grid} beyond certain thresholds, while amplifications are expected to reduce monotonically with increasing B values.

Tests were conducted using a representative extreme focusing scenario (configuration T2, $T = 10$ s, $\theta_{\rm rel} = 170°$). Near-opposing conditions generate the sharpest refractive gradients and are therefore the most sensitive to numerical under-resolution. The peak wave amplification (A/A_0) was tracked across all parameter variations, as shown in Fig. 27, with the corresponding spatial amplification fields illustrated in Figs. 28 to 30.

As illustrated in Fig. 27a, the maximum wave amplification remains remarkably stable across the entire range of injected rays tested ($250 \leq N_{\rm rays} \leq 1500$). The spatial fields shown in Fig. 28 further demonstrate that the overall refractive pattern, including the lateral focal zones, are fully captured even at the lowest seeding densities tested here. The variation in A/A_0 is extremely small (less than 1%), indicating that the baseline of $N_{\rm rays} = 1000$ provides reliable results significantly beyond the threshold for convergence.

Fig. 27b illustrates the sensitivity to the background velocity grid resolution. Coarser grids ($N_{\rm grid} < 600$) may fail to resolve the sharpest lateral shear transitions, which can lead to sharper velocity edges and higher refractive focusing in extreme cases. However, as shown in the

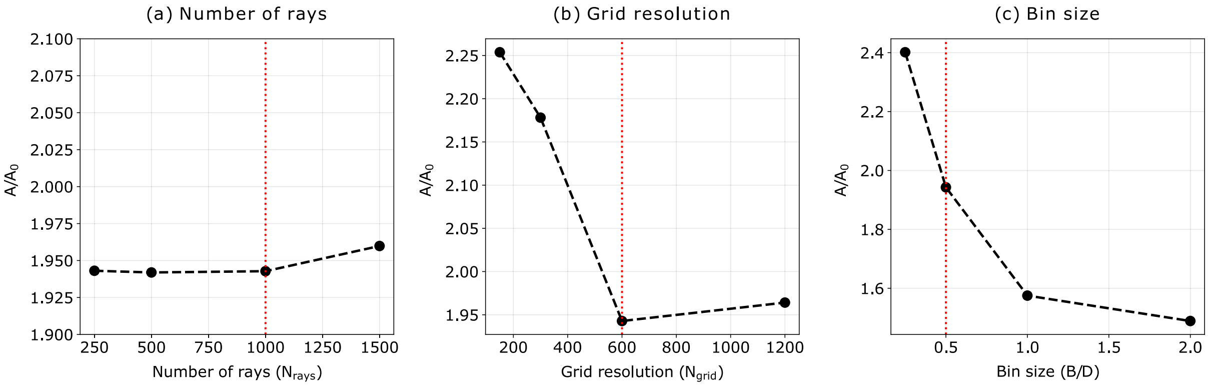

Fig. 27. Numerical sensitivity of the maximum spatially averaged wave amplification (A/A_0) for a representative extreme focusing case ($T = 10$ s, $\theta_{\mathrm{rel}} = 170°$). Sensitivity is assessed for (a) the number of rays N_{rays}, (b) the grid resolution N_{grid}, and (c) the bin size B/D. Vertical red dotted lines indicate the baseline parameters used in this study.

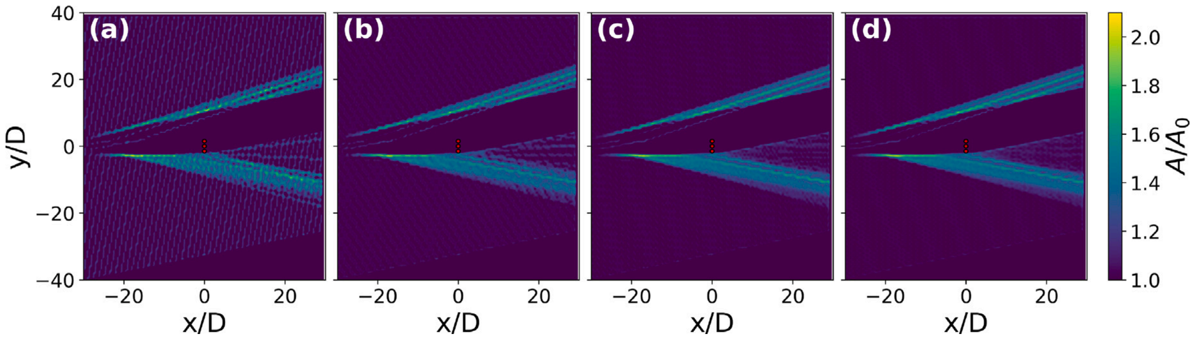

Fig. 28. Sensitivity of the spatial wave amplification field A/A_0 to the number of injected rays N_{rays}: (a) 250, (b) 500, (c) 1000 (baseline), and (d) 1500 rays.

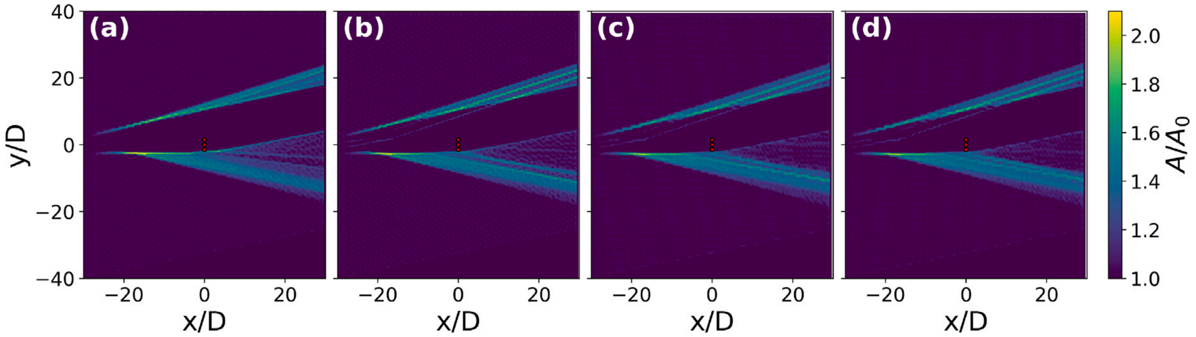

Fig. 29. Sensitivity of the spatial wave amplification field A/A_0 to the background velocity grid resolution N_{grid}: (a) 150, (b) 300, (c) 600 (baseline), and (d) 1200 points.

spatial comparisons in Fig. 29, the results demonstrate clear convergence at $N_{\mathrm{grid}} = 600$ used in this study. Refinement to 1200 points yields negligible changes to the resulting focal patterns, confirming that the spatial gradients of the current field are fully resolved.

The sensitivity to the spatial averaging bin size, B, for amplification fields is shown in Fig. 27c and visualised spatially in Fig. 30. Unlike the purely numerical parameters above, this represents a physical binning/smoothing choice. Because wave-ray tracing calculates infinitesimal ray paths, the local wave action density must be calculated by counting rays within a finite area. As seen in Fig. 30, smaller bins (e.g., $0.25D$) capture highly localised caustic peaks with high variance, while larger bins (e.g., $2.0D$) significantly smooth these peaks over a wider area. In this study, the bin size is fixed to $B = R$ (or $B/D = 0.5$) to represent a spatial filter of the scale of importance for TST rotors.

Appendix B. Theoretical estimates of model error

B.1. Reflection and transmission errors

To gauge the amplitude error introduced by ray–tracing assumptions, we consider two limiting cases for rays that cross the wake centreline.

B.1.1. Sharp velocity step

In an idealised step model the effective current changes instantaneously between the freestream and the wake centre. Across this interface we need to have (i) continuity of surface elevation and (ii) conservation of wave-action flux $(E/\sigma)c_g$ (Bretherton and Garrett,

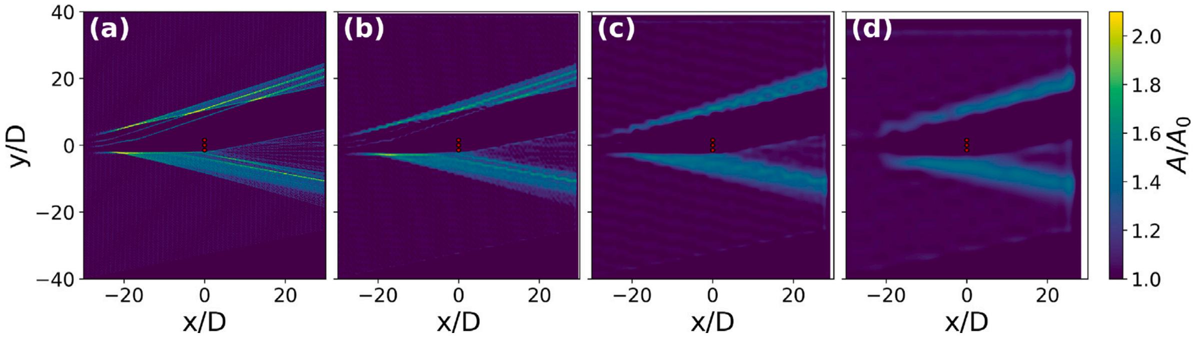

Fig. 30. Sensitivity of the spatial wave amplification field A/A_0 to the spatial averaging bin size B/D: (a) 0.25, (b) 0.5 (baseline), (c) 1.0, and (d) 2.0.

1968; Peregrine, 1976). Writing the complex Fourier coefficients as $\hat{\eta}_i$ (incident), $\hat{\eta}_r$ (reflected), and $\hat{\eta}_t$ (transmitted), condition (i) at the interface gives

$$\hat{\eta}_i + \hat{\eta}_r = \hat{\eta}_t. \tag{18}$$

With $E \propto |\hat{\eta}|^2$ and the interface normal directed from region i to t, the action–flux balance is

$$\mathcal{Y}_i\left(|\hat{\eta}_i|^2 - |\hat{\eta}_r|^2\right) = \mathcal{Y}_t\,|\hat{\eta}_t|^2, \qquad \mathcal{Y} = \frac{c_{g,abs}}{\sigma}. \tag{19}$$

where the sign for the action for the reflected wave is negative due to having a negative group velocity. Note that some formulations for wave action flux use $(E/\sigma)(c_g + U)$ (e.g. Peregrine, 1976), but we use the absolute group velocity $c_{g,abs} = \partial\omega/\partial k$ with $\omega = \sigma(k) + kU$, which includes the mean flow U into the advection of wave action across the interface.

The reflection and transmission amplitude coefficients are defined as:

$$K_{r,step} = \frac{\hat{\eta}_r}{\hat{\eta}_i}, \qquad K_{t,step} = \frac{\hat{\eta}_t}{\hat{\eta}_i}. \tag{20}$$

Dividing (18) by $\hat{\eta}_i$ we have $K_{t,step} = 1 + K_{r,step}$. Substituting into (19) and solving yields

$$K_{r,step} = \frac{\mathcal{Y}_i - \mathcal{Y}_t}{\mathcal{Y}_i + \mathcal{Y}_t}, \qquad K_{t,step} = \frac{2\,\mathcal{Y}_i}{\mathcal{Y}_i + \mathcal{Y}_t}. \tag{21}$$

This is analogous to admittance matching in electrical engineering, with $\mathcal{Y}$ playing the role of an admittance, see e.g., (Pozar, 1998, Eq. (2.51)). To assess the error from the wave-ray tracing assumption of perfect transmission, we assess the transmission coefficient $K_{t,step}$ where values greater than unity represent amplification and values less than units represent amplitude reduction, both of which are omitted using the wave ray tracing approach.

B.1.2. Smooth (no-reflection) limit

If the velocity varies smoothly so that no reflection occurs, conservation of action flux, $(Ec_{g,abs}/\sigma)_i = (Ec_{g,abs}/\sigma)_t$ along a ray gives the amplitude ratio

$$K_{t,smooth} = \frac{|\hat{\eta}_t|}{|\hat{\eta}_i|} = \sqrt{\frac{(\sigma/c_{g,abs})_t}{(\sigma/c_{g,abs})_i}} = \sqrt{\frac{\mathcal{Y}_i}{\mathcal{Y}_t}}, \tag{22}$$

noting that this local amplitude adjustment (via action conservation) is not included in the wave-ray tracing approach used here. We assess $K_{t,smooth}$ to understand the potential maximum errors associated with using the wave ray tracing approach.

B.1.3. Relation between limits

Defining $r = \mathcal{Y}_t/\mathcal{Y}_i > 0$, then we can write $K_{t,step} = 2/(1 + r)$ and $K_{t,smooth} = 1/\sqrt{r}$. It can be readily seen that

$$K_{t,step} \leq K_{t,smooth} \quad \text{for all } r > 0 \text{ (i.e. there is a wave transmitted)}, \tag{23}$$

which are only equal when $r = 1$ (i.e. the wave is entirely transmitted). Thus the transmitted amplitude (and the signed error metric $\epsilon = K_t - 1$) for a sharp step is always less than the smooth (no-reflection) value as would make intuitive sense. In practice, the physical result is expected to be between these two values.

B.2. Wave power change

We now outline the derivation of the expressions used in Section 4.2.2.

We consider collinear wave–current–turbine interactions, so the rotor axis and the wave propagation direction coincide. Hence the turbine thrust acts along the wave direction. The instantaneous flow along this axis is the sum $U_e + u(t)$, where U_e is positive for following currents and negative for opposing currents, and is assumed uniform with depth here. The turbine thrust is modelled quasi-steadily with a constant thrust coefficient C_T as:

$$T(t) = \frac{1}{2}\rho A C_T\left(U_e + u(t)\right)^2, \tag{24}$$

where $u(t)$ is the time-varying rotor-averaged wave-induced velocity component.

The wave-induced horizontal velocity amplitude (i.e. omitting time variation) as a function of z is:

$$u_1(z) = \frac{gak}{\sigma(k)}\,\frac{\cosh\!\big(k(z+h)\big)}{\cosh(kh)} \tag{25}$$

The corresponding root mean square (RMS) value is $u_{1,rms}(z) = u_1(z)/\sqrt{2}$.

Following the weighting for a circular disc (e.g. Draycott et al., 2019b), the rotor-average of any quantity $q(z)$ is

$$\langle q\rangle_{rotor} = \frac{\int_{z_0-R}^{z_0+R} q(z)w(z)\,dz}{\int_{z_0-R}^{z_0+R} w(z)\,dz}, \qquad w(z) = 2\sqrt{R^2 - (z-z_0)^2}. \tag{26}$$

Hence,

$$\left\langle u^2\right\rangle_{rotor} = \left\langle u_{1,rms}^2\right\rangle_{rotor} = \frac{1}{2}\left\langle (u_1)^2\right\rangle_{rotor}. \tag{27}$$

The instantaneous power transfer between the wave field and the turbine is $\Delta P(t) = T(t)\,u(t)$. Averaging over a cycle and retaining the leading contribution gives

$$\left\langle \Delta P\right\rangle = \rho A C_T\, U_e \left\langle u^2\right\rangle_{rotor}. \tag{28}$$

The sign of the mean exchange is therefore set by U_e: following ($U_e > 0$) yields damping (power loss from the waves), while opposing ($U_e < 0$) can produce a small amplification (power gain to the waves) by transferring energy from the mean current to the waves.

We compare the power change given in (28) to the incoming wave power. The wave power per unit crest length is:

$$p = Ec_{g,abs}, \qquad E = \frac{1}{2}\rho g a^2 \tag{29}$$

and use the crest length of relevance equal the rotor diameter, $L = 2R$, so

$$P_0 = pL = \left(\frac{1}{2}\rho g a^2\right) c_{g,abs}(2R). \tag{30}$$

From (25) to (27), $\langle u^2\rangle_{rotor} \propto a^2$, hence

$$\frac{\Delta P}{P_0} = \frac{\rho A C_T U_e \langle u^2\rangle_{rotor}}{\left(\frac{1}{2}\rho g a^2\right) c_{g,abs}(2R)} = \frac{A C_T U_e \left\langle u^2_{1,rms}\right\rangle_{rotor}[a=1]}{g\, c_{g,abs}\, R}, \tag{31}$$

where $\left\langle u^2_{1,rms}\right\rangle_{rotor}[a=1]$ is computed with unit surface amplitude and includes the rotor weighting (Eq. (26)). Eq. (31) shows that the a^2 cancels, so $\Delta P/P_0$ is not amplitude dependent under linear wave theory.

Since wave power scales as $P \propto a^2$, the relative amplitude change can be calculated as:

$$\frac{a_{\text{out}}}{a_{\text{in}}} = \sqrt{1 - \frac{\Delta P}{P_0}} \tag{32}$$

so that $a_{\text{out}}/a_{\text{in}} > 1$ corresponds to a slight amplification when $\Delta P/P_0 < 0$ (opposing).

It is worth noting that the $\Delta P/P_0$ in (31) is a local measure. We normalise the incident wave power by a crest length equal to the rotor diameter, $L = 2R$, so $P_0 = E\, c_{g,abs}(2R)$. Thus, ΔP quantifies the mean work exchanged as the waves traverse one rotor disc. Diffraction effects are not included in this local estimate and will act to reduce the observed change (positively or negatively) in the local amplitude.

Data availability

No data was used for the research described in the article.

References

Adcock, T.A., Draper, S., Houlsby, G.T., Borthwick, A.G., Serhadıoğlu, S., 2013. The available power from tidal stream turbines in the pentland firth. Proc. R. Soc. A 469, 20130072.

Apsley, D.D., 2024. Cfd simulation of tidal-stream turbines in a compact array. Renew. Energy 224, 120133.

Apsley, D.D., Stallard, T., Stansby, P.K., 2018. Actuator-line CFD modelling of tidal-stream turbines in arrays. J. Ocean Eng. Marine Energy 4, 259–271.

Babanin, A.V., Van der Weshuijsen, A., Chalikov, D., Rogers, W.E., 2017. Advanced wave modeling, including wave–current interaction.

Barltrop, N., Varyani, K., Grant, A., Clelland, D., Pham, X., 2006. Wave–current interactions in marine current turbines. Proc. Inst. Mech. Eng. M 220, 195–203.

Barnes, M.A., Rautenbach, C., 2020. Toward operational wave–current interactions over the agulhas current system. J. Geophys. Res.: Ocean. 125, e2020JC016321.

Bretherton, F.P., Garrett, C.J.R., 1968. Wavetrains in inhomogeneous moving media. Proc. R. Soc. Lond. A 302, 529–554.

Coles, D., Angeloudis, A., Greaves, D., Hastie, G., Lewis, M., Mackie, L., McNaughton, J., Miles, J., Neill, S., Piggott, M., et al., 2021. A review of the uk and british channel islands practical tidal stream energy resource. Proc. R. Soc. A 477, 20210469.

de Jesus Henriques, T., Tedds, S., Botsari, A., Najafian, G., Hedges, T., Sutcliffe, C., Owen, I., Poole, R., 2014. The effects of wave–current interaction on the performance of a model horizontal axis tidal turbine. Int. J. Mar. Energy 8, 17–35.

de Leon, S.P., Soares, C.G., 2022. Numerical study of the effect of current on waves in the agulhas current retroflection. Ocean Eng. 264, 112333.

Draycott, S., Nambiar, A., Sellar, B., Davey, T., Venugopal, V., 2019a. Assessing extreme loads on a tidal turbine using focused wave groups in energetic currents. Renew. Energy 135, 1013–1024.

Draycott, S., Payne, G., Steynor, J., Nambiar, A., Sellar, B., Venugopal, V., 2019b. An experimental investigation into non-linear wave loading on horizontal axis tidal turbines. J. Fluids Struct. 84, 199–217.

Draycott, S., Steynor, J., Nambiar, A., Sellar, B., Venugopal, V., 2019c. Experimental assessment of tidal turbine loading from irregular waves over a tidal cycle. J. Ocean. Eng. Mar. Energy 5, 173–187.

Draycott, S., Steynor, J., Nambiar, A., Sellar, B., Venugopal, V., 2020a. Rotational sampling of waves by tidal turbine blades. Renew. Energy 162, 2197–2209.

Draycott, S., Steynor, J., Nambiar, A., Sellar, B., Venugopal, V., 2020b. Tidal turbine load variability in following and opposing irregular wave conditions. In: International Conference on Offshore Mechanics and Arctic Engineering. Vol. 84416, American Society of Mechanical Engineers, V009T09A004.

Faudot, C., Dahlhaug, O.G., 2012. Prediction of wave loads on tidal turbine blades. Energy Procedia 20, 116–133.

Funke, S.W., Farrell, P.E., Piggott, M.D., 2014. Tidal turbine array optimisation using the adjoint approach. Renew. Energy 63, 658–673.

Galloway, P.W., Myers, L.E., Bahaj, A.S., 2014. Quantifying wave and yaw effects on a scale tidal stream turbine. Renew. Energy 63, 297–307.

Gaurier, B., Davies, P., Deuff, A., Germain, G., 2013. Flume tank characterization of marine current turbine blade behaviour under current and wave loading. Renew. Energy 59, 1–12.

Gaurier, B., Ordonez-Sanchez, S., Facq, J.-V., Germain, G., Johnstone, C., Martinez, R., Salvatore, F., Santic, I., Davey, T., Old, C., Sellar, B., 2020. MaRINET2 tidal energy round robin tests—Performance comparison of a horizontal axis turbine subjected to combined wave and current conditions. J. Mar. Sci. Eng. 8 (6), 463.

Halsne, T., Christensen, K.H., Hope, G., Breivik, Ø., 2023. Ocean wave tracing v. 1: a numerical solver of the wave ray equations for ocean waves on variable currents at arbitrary depths. Geosci. Model. Dev. 16, 6515–6530.

Halsne, T., Li, Y., 2025. Coastal wave refraction in variable currents over a varying bathymetry. arXiv preprint arXiv:2501.07132.

Hashemi, M.R., Neill, S.P., Robins, P.E., Davies, A.G., Lewis, M.J., 2015. Effect of waves on the tidal energy resource at a planned tidal stream array. Renew. Energy 75, 626–639.

Hasselmann, K., Barnett, T.P., Bouws, E., Carlson, H., Cartwright, D.E., Enke, K., Ewing, J., Gienapp, A., Hasselmann, D., Kruseman, P., et al., 1973. Measurements of wind-wave growth and swell decay during the joint north sea wave project (jonswap). Ergaenzungsheft Dtsch. Hydrogr. Z. Reihe A.

Hedges, T., Lee, B., 1992. The equivalent uniform current in wave–current computations. Coast. Eng. 16, 301–311.

Hurubi, S., Ouro, P., Stansby, P., Stallard, T., 2025. Influence of seabed irregularity on the wake of a tidal turbine. Phys. Fluids 37.

Johnson, J., 1947. The refraction of surface waves by currents. Eos Trans. Am. Geophys. Union 28, 867–874.

Jonsson, I.G., Wang, J.D., 1980. Current-depth refraction of water waves. Ocean Eng. 7, 153–171.

Li, Y., Chabchoub, A., 2024. How currents trigger extreme sea waves. the roles of stokes drift, eulerian return flow, and a background flow in the open ocean. Ocean. Geophys. Res. Lett. 51, e2023GL107381.

Li, Y., Ellingsen, S.Å., 2019. A framework for modeling linear surface waves on shear currents in slowly varying waters. J. Geophys. Res.: Ocean. 124, 2527–2545.

Li, Z., Ghia, K., Li, Y., Fan, Z., Shen, L., 2021. Unsteady Reynolds-averaged Navier–Stokes investigation of free surface wave impact on tidal turbine wake. Proc. R. Soc. A 477, 20200703.

Longuet-Higgins, M.S., Stewart, R., 1962. Radiation stress and mass transport in gravity waves, with application to 'surf beats'. J. Fluid Mech. 13, 481–504.

Lu, J., Wang, L.-L., Tang, H.-W., Dai, H.-C., 2011. Large eddy simulation of vertical turbulent jets under jonswap waves. Acta Mech. Sin. 27, 189–199.

Lust, E.E., Luznik, L., Flack, K.A., Walker, J.M., Van Benthem, M.C., 2013. The influence of surface gravity waves on marine current turbine performance. Int. J. Mar. Energy 3, 27–40.

Luznik, L., Flack, K.A., Lust, E.E., Taylor, K., 2013. The effect of surface waves on the performance characteristics of a model tidal turbine. Renew. Energy 58, 108–114.

MacIver, R., Simons, R., Thomas, G., 2006. Gravity waves interacting with a narrow jet-like current. J. Geophys. Res.: Ocean. 111.

Mackay, E.B., Hardwick, J.P., 2022. Joint extremes of waves and currents at tidal energy sites in the english channel. In: International Conference on Offshore Mechanics and Arctic Engineering. Vol. 85932, American Society of Mechanical Engineers, V008T09A003.

Martinez, R., Ordonez-Sanchez, S., Allmark, M., Lloyd, C., O'Doherty, T., Germain, G., Gaurier, B., Johnstone, C., 2020. Analysis ofthe effects ofcontrol strategies and wave climates on the loading and performance ofa laboratory scale horizontal axis tidal turbine. J. Mar. Sci. Eng. 212, 107713.

McAllister, M., Draycott, S., Calvert, R., Davey, T., Dias, F., van den Bremer, T., 2024. Three-dimensional wave breaking. Nature 633, 601–607.

Mullings, H., Amos, L., Miller, C., Ouro, P., Stallard, T., 2024. Efficient prediction of tidal turbine fatigue loading using turbulent onset flow from large eddy simulations. J. Ocean. Eng. Mar. Energy 10, 537–554.

Myers, L., Bahaj, A., 2012. An experimental investigation simulating flow effects in first generation marine current energy converter arrays. Renew. Energy 37, 28–36.

Nambiar, A., Draycott, S., Payne, G.S., Sellar, B., Kiprakis, A., 2021. Influence of tidal turbine control on performance and loads. Appl. Ocean Res. 114, 102806.

Nishino, T., Willden, R.H., 2012. The efficiency of an array of tidal turbines partially blocking a wide channel. J. Fluid Mech. 708, 596–606.

Noble, D.R., Draycott, S., Nambiar, A., Sellar, B.G., Steynor, J., Kiprakis, A., 2020. Experimental assessment of flow, performance, and loads for tidal turbines in a closely-spaced array. Energies 13, 1977.

Olczak, A., 2016. The Influence of Waves on Tidal Stream Turbine Arrays (Ph.D. thesis). The University of Manchester, United Kingdom.

Olczak, A., Stallard, T., Feng, T., Stansby, P., 2016. Comparison of a rans blade element model for tidal turbine arrays with laboratory scale measurements of wake velocity and rotor thrust. J. Fluids Struct. 64, 87–106.

Ordonez-Sanchez, S., Allmark, M., Porter, K., Ellis, R., Lloyd, C., Santic, I., O'Doherty, T., Johnstone, C., 2019. Analysis of a horizontal-axis tidal turbine performance in the presence of regular and irregular waves using two control strategies. Energies 367, 12(3).

Ouro, P., Dené, P., Garcia-Novo, P., Stallard, T., Kyozuda, Y., Stansby, P., 2023. Power density capacity of tidal stream turbine arrays with horizontal and vertical axis turbines. J. Ocean. Eng. Mar. Energy 9, 203–218.

Ouro, P., Mullings, H., Christou, A., Draycott, S., Stallard, T., 2024. Wake characteristics behind a tidal turbine with surface waves in turbulent flow analyzed with large-eddy simulation. Phys. Rev. Fluids 9, 034608.

Ouro, P., Nishino, T., 2021. Performance and wake characteristics of tidal turbines in an infinitely large array. J. Fluid Mech. 925, A30.

Ouro, P., Ramírez, L., Harrold, M., 2019. Analysis of array spacing on tidal stream turbine farm performance using large-eddy simulation. J. Fluids Struct. 91, 102732.

Peregrine, D.H., 1976. Interaction of water waves and currents. Adv. Appl. Mech. 16, 9–117.

Peregrine, D.H., Jonsson, I.G., 1983. Interaction of waves and currents.

Posa, A., Broglia, R., 2021. Characterization of the turbulent wake of an axial-flow hydrokinetic turbine via large-eddy simulation. Comput. Fluids 216, 104815.

Posa, A., Broglia, R., 2022. Analysis of the momentum recovery in the wake of aligned axial-flow hydrokinetic turbines. Phys. Fluids 34, 105130.

Pozar, D.M., 1998. Microwave Engineering, second ed. University of Massachusetts at Amherst, John Wiley & Sons, Inc.

Quilfen, Y., Yurovskaya, M., Chapron, B., Ardhuin, F., 2018. Storm waves focusing and steepening in the agulhas current: Satellite observations and modeling. Remote Sens. Environ. 216, 561–571.

Rapizo, H., Babanin, A., Gramstad, O., Ghantous, M., 2014. Wave refraction on southern ocean eddies. In: Proc. 19th Australasian Fluid Mechanics Conf. pp. 1–4.

Sabatino, A.D., McCaig, C., O'Hara Murray, R.B., Heath, M.R., 2016. Modelling wave–current interactions off the east coast of scotland. Ocean. Sci. 12, 875–897.

Sellar, B.G., Wakelam, G., Sutherland, D.R., Ingram, D.M., Venugopal, V., 2018. Characterisation of tidal flows at the european marine energy centre in the absence of ocean waves. Energies 11, 176.

Shi, F., Kirby, J.T., Harris, J.C., Geiman, J.D., Grilli, S.T., 2012. A high-order adaptive time-stepping tvd solver for boussinesq modeling of breaking waves and coastal inundation. Ocean. Model. 43, 36–51.

Smith, J.A., 2006. Wave–current interactions in finite depth. J. Phys. Oceanogr. 36, 1403–1419.

Stallard, T., Collings, R., Feng, T., Whelan, J., 2013. Interactions between tidal turbine wakes: experimental study of a group of three-bladed rotors. Philos. Trans. R. Soc. A 371, 20120159.

Stallard, T., Feng, T., Stansby, P., 2015. Experimental study of the mean wake of a tidal stream rotor in a shallow turbulent flow. J. Fluids Struct. 54, 235–246.

Stallard, T., Mullings, H., Draycott, S., Ouro, P., 2023. Large-eddy simulations of interaction between surface waves and a tidal turbine wake in a turbulent channel. In: Proceedings of the 15th European Wave and Tidal Energy Conference. EWTEC.

Stansby, P., Moreno, E.C., Draycott, S., Stallard, T., 2022. Total wave power absorption by a multi-float wave energy converter and a semi-submersible wind platform with a fast far field model for arrays. J. Ocean. Eng. Mar. Energy 8, 43–63.

Stansby, P.K., Ouro, P., 2022. Modelling marine turbine arrays in tidal flows. J. Hydraul. Res. 60, 187–204.

Stansby, P., Stallard, T., 2016. Fast optimisation of tidal stream turbine positions for power generation in small arrays with low blockage based on superposition of self-similar far-wake velocity deficit profiles. Renew. Energy 92, 366–375.

Tatum, S., Allmark, M., Frost, C., O'Doherty, D., Mason-Jones, A., O'Doherty, T., 2016. CFD modelling of a tidal stream turbine subjected to profiled flow and surface gravity waves. Int. J. Mar. Energy 15, 156–174.

Tatum, S.C., Frost, C.H., Allmark, M., O'Doherty, D.M., Mason-Jones, A., Prickett, P.W., Grosvenor, R.I., Byrne, C.B., O'Doherty, T., 2016. Wave–current interaction effects on tidal stream turbine performance and loading characteristics. Int. J. Mar. Energy 14, 161–179.

Toffoli, A., Cavaleri, L., Babanin, A., Benoit, M., Bitner-Gregersen, E., Monbaliu, J., Onorato, M., Osborne, A.R., Stansberg, C., 2011. Occurrence of extreme waves in three-dimensional mechanically generated wave fields propagating over an oblique current. Nat. Hazards Earth Syst. Sci. 11, 895–903.

Yang, Y., Draycott, S., Stansby, P.K., Rogers, B.D., 2023a. A numerical flume for waves on variable sheared currents using smoothed particle hydrodynamics (sph) with open boundaries. Appl. Ocean Res. 135, 103527.

Yang, Y., Stansby, P.K., Rogers, B.D., Buldakov, E., Stagonas, D., Draycott, S., 2023b. The loading on a vertical cylinder in steep and breaking waves on sheared currents using smoothed particle hydrodynamics. Phys. Fluids 35.

Zang, W., Zhang, Y., Zheng, Y., Zhang, J., Guan, D., Fernandez-Rodriguez, E., 2023. On the impact of waves and turbulence on the power fluctuations and wake structure of a tidal-stream turbine. Phys. Fluids 35, 055115.

Zhang, Y., Zang, W., Zheng, J., Cappietti, L., Zhang, J., Zheng, Y., Fernandez-Rodriguez, E., 2021. The influence of waves propagating with the current on the wake of a tidal stream turbine. Appl. Energy 290, 116729.